Zang, A., Stephansson, O., Stenberg, L., Plenkers, K., Specht, S., Milkereit, C., Schill, E., Kwiatek, G., Dresen, G., Zimmermann, G., Dahm, T., Weber, M. (2016): Hydraulic fracture monitoring in hard rock at 410 m depth with an advanced fluid-injection protocol and extensive sensor array. - *Geophysical Journal International*, *208*, 2, pp. 790—813.

DOI: http://doi.org/10.1093/gji/ggw430

Geophysical Journal International

Geophys. J. Int. (2017) **208,** 790–813
Advance Access publication 2016 November 17
GJI Seismology

doi: 10.1093/gji/ggw430

Hydraulic fracture monitoring in hard rock at 410 m depth with an advanced fluid-injection protocol and extensive sensor array

Arno Zang,[1,2] Ove Stephansson,[1] Leif Stenberg,[3] Katrin Plenkers,[4] Sebastian Specht,[1,2] Claus Milkereit,[1] Eva Schill,[5] Grzegorz Kwiatek,[1] Georg Dresen,[1,2] Günter Zimmermann,[1] Torsten Dahm[1,2] and Michael Weber[1,2]

[1] *GFZ German Research Center for Geosciences, Potsdam, Germany. E-mail: zang@gfz-potsdam.de*
[2] *Institute of Earth and Environmental Sciences, University of Potsdam, Potsdam, Germany*
[3] *SKB Swedish Nuclear Fuel and Waste Management Co., Oskarshamn, Sweden*
[4] *GMuG Gesellschaft für Materialprüfung und Geophysik mbH, Bad Nauheim, Germany*
[5] *KIT Karlsruhe Institute of Technology, Reservoir Technology, Karlsruhe, Germany*

Accepted 2016 November 14. Received 2016 October 14; in original form 2016 April 25

SUMMARY

In this paper, an underground experiment at the Äspö Hard Rock Laboratory (HRL) is described. Main goal is optimizing geothermal heat exchange in crystalline rock mass at depth by multistage hydraulic fracturing with minimal impact on the environment, that is, seismic events. For this, three arrays with acoustic emission, microseismicity and electromagnetic sensors are installed mapping hydraulic fracture initiation and growth. Fractures are driven by three different water injection schemes (continuous, progressive and pulse pressurization). After a brief review of hydraulic fracture operations in crystalline rock mass at mine scale, the site geology and the stress conditions at Äspö HRL are described. Then, the continuous, single-flow rate and alternative, multiple-flow rate fracture breakdown tests in a horizontal borehole at depth level 410 m are described together with the monitoring networks and sensitivity. Monitoring results include the primary catalogue of acoustic emission hypocentres obtained from four hydraulic fractures with the *in situ* trigger and localizing network. The continuous versus alternative water injection schemes are discussed in terms of the fracture breakdown pressure, the fracture pattern from impression packer result and the monitoring at the arrays. An example of multistage hydraulic fracturing with several phases of opening and closing of fracture walls is evaluated using data from acoustic emissions, seismic broad-band recordings and electromagnetic signal response. Based on our limited amount of *in situ* tests (six) and evaluation of three tests in Ävrö granodiorite, in the multiple-flow rate test with progressively increasing target pressure, the acoustic emission activity starts at a later stage in the fracturing process compared to the conventional fracturing case with continuous water injection. In tendency, also the total number and magnitude of acoustic events are found to be smaller in the progressive treatment with frequent phases of depressurization.

Key words: Geomechanics; Fracture and flow; Broad-band seismometers.

1 INTRODUCTION

Hydraulic fracturing (HF) is a technique in which a fluid (e.g. water) is injected into a borehole at high pressure in order to induce fractures into the surrounding rocks. This operation is a key mechanism to increase the permeability of rock, to enhance fluid productivity of tight rock and, therefore, to improve energy extraction in geothermal and hydrocarbon exploitation. HF for enhanced geothermal systems, shale gas and conventional oil and gas extraction has become a major research and engineering topic in a large variety of geological conditions (e.g. Economides *et al.* 2000). However, the process imposes environmental risks, one of which is induced seismicity accompanying hydraulic fracture growth (Ellsworth 2013; Rubinstein & Mahani 2015). Of particular interest are fracturing concepts that limit the number and magnitudes of induced seismic events. In this context, based on numerical modelling of laboratory results, the fatigue HF (FHF) concept has been introduced (Zang *et al.* 2013) to mitigate seismicity while the permeability enhancement process is preserved. However, modelling the HF process and associated induced seismicity is highly nonlinear and a complex process (Smart *et al.* 2014). Based on laboratory test results, Yoon *et al.* (2014) developed and calibrated a hydromechanically coupled modelling tool which is able to study the application of FHF for dynamic cyclic and pulse injection treatments.

During cyclic injection the fluid pressure is lowered frequently to allow stress relaxation at the fracture tip possibly causing a lower number and magnitude of induced seismic events in fatigue testing. Moreover, cyclic injection appears to provide comparably efficient permeability enhancement (Patel *et al.* 2016). So far, field tests validating the postulated seismic response of hydraulic fracture nucleation and growth for different fluid injection scenarios are missing.

There are different scales involved in hydraulic treatments of rock mass. Whereas HF operations in hydrocarbon (Suckale 2009) and geothermal (Zang *et al.* 2014) exploitation cover rock volumes of several hundreds of metres, HF on mine scale normally extend over a few tens of metres only. Microseismicity (MS) and *in situ* acoustic emission (AE) systems were used to monitor HF at mine scale. Electromagnetic (EM) monitoring hitherto has been applied at reservoir or larger scale, only.

Attempts have been made to map hydraulic fracture growth in mines both with low frequency (5 Hz to 100 Hz) and high frequency (100 Hz to 500 Hz) MS monitoring systems. Manthei & Eisenblätter (2008) reviewed AE and MS monitoring experiments in mines related to excavation and hydraulic fracture growth. Recently for oil industry purpose, Jeffrey *et al.* (2009) reported on measuring hydraulic fracture growth in naturally fractured, crystalline rock at a depth of 580 m in Northpakes Mines, Australia. In their study, a combination of tiltmeter and MS arrays (triaxial accelerometers) were installed to determine fracture growth, which was followed by mine-through mapping. Due to a lack of recorded events, MS monitoring failed to image hydraulic fractures. Nevertheless, hydraulic fracture growth could be followed by low frequency tiltmeter data and inspection of excavated fracture walls filled with proppants distributed with the injection fluid.

During HF, very weak seismic events, that is, AE or the so-called picoseismicity [magnitude range −4 to −2, Bohnhoff *et al.* (2009, table 1 therein)], often accompany close to the tip of a fracture, and have been used to measure the orientation and growth velocity of the fractures (Fischer *et al.* 2009). Although Eisenblätter (1988) demonstrated that AE monitoring with frequencies between 1 and 100 kHz can be used to locate the size and orientation of HF in salt rock, AE monitoring of hydraulic fractures at mine scale is rare, in particular in hard crystalline rock (Niitsuma *et al.* 1993). On one hand, this originates from the kHz range of AE posing significant demands on the recording units and has improved recently. On the other hand, seismic waves in the kHz frequency range may be strongly damped, and therefore sensors need to be located very close to the HF experiment. Accordingly, the number of AE recorded during fracture growth crucially depends on the rock type, the damping mechanism and the volume of fluid injected. For example, in rock salt at Bernburg mine (Germany), Manthei *et al.* (2003) reported 15 000 AE during the growth of four hydraulic fractures. Dahm & Krüger (1999) and Dahm (2001) analysed the source mechanism and rupture of these induced AE events from HF and conclude that the events are clearly associated to shear cracks in the close vicinity of the fractures. On the other hand, Niitsuma *et al.* (1993) found only 234 AE associated with four hydraulic fracture tests in crystalline rock at depth in Kamaishi mine, Japan. AE sensors are often beneficial over high frequency seismometers in the kHz range, because they are much more sensitive.

Guglielmi *et al.* (2015) studied fault movements and seismicity induced over time by fluid injection and simultaneous recording of the fault displacement with a displacement sensor installed in a borehole of a limestone formation in France. Fluid injection primarily triggered aseismic slip while low cumulative fault normal displacement and microearthquakes and fault slip developed during late stage of pressurization.

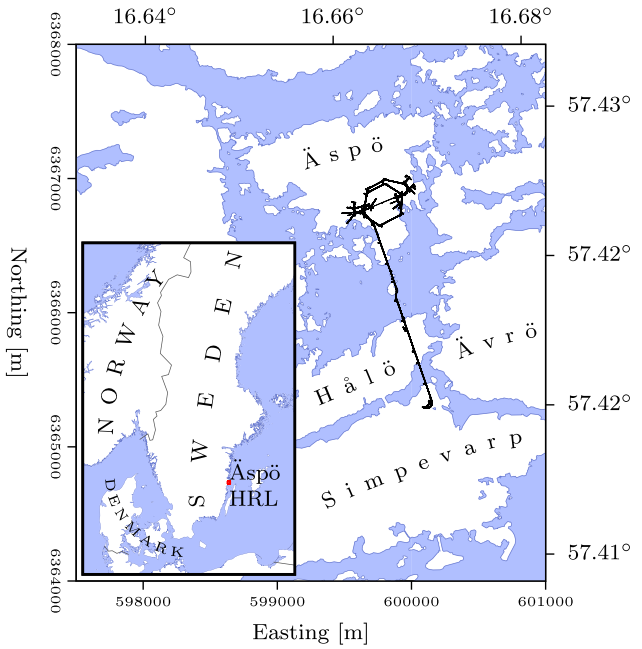

Figure 1. Location of Äspö Hard Rock Laboratory (HRL) in the south of Sweden, approximately 35 km north of the city of Oskarshamn.

EM monitoring is a rather recent development in reservoir engineering. It bases on observations of natural processes prior to earthquakes. As such electrokinetic effects, occurring when fluid flows through fractures, have been observed during deformation prior to earthquakes and attributed to fluid percolation in the crust, driven by pore pressure gradients (Mizutani *et al.* 1976). Dilation is assumed to enhance the permeability near a natural fault (Murakami *et al.* 1984). Electrokinetic phenomena were observed also during water injection experiments. Increasing electric self-potential was observed, for example, in the Nojima fault under flow rates in the order of 0.17–0.33 L s^{-1} and pressure changes up to 4 MPa (Murakami *et al.* 2008). The electrokinetic origin of transient signals in the electric and magnetic field prior to the Loma Prieta earthquake in 1989 (Fenoglio 1995) suggest that high pore pressure changes can be monitored also using magnetotelluric (MT) methods. In engineered reservoirs, self-potential changes in the order of several mV were observed under flow rates in the order of up to 50 L s^{-1} and pressure changes up to 12 MPa at the Soultz-sous-Forêts EGS site including a pressure dependent peak in the shut-in phase (Darnet *et al.* 2004). An injection of 3100 m^3 of brine with a flow rate up to 30 L s^{-1} and pressures up to 62 MPa into metasediments at 3680 m depth in well Paralana 2 (South Australia), shows coherent and significant variation in EM parameters such as the phase tensor in space and time (Peacock *et al.* 2012).

In this study, a field test is described operated during May and June 2015 in Äspö Hard Rock Laboratory (HRL) located approximately 35 km north of the city of Oskarshamn, Sweden (Fig. 1). The field setup was designed to test the FHF concept with alternative water injection schemes on mine scale with advanced fluid injection protocols and extensive sensor arrays. Six HF experiments with three different water injection schemes (continuous, progressive and pulse pressurization) in crystalline rock at 410 m depth were monitored simultaneously with AE, MS, broad-band and EM sensors. The Äspö HRL has been selected because geology, hydraulics and

Table 1. Overview of used symbols and abbreviations.

AE	Acoustic emission
EM(E)	Electromagnetic (Emission)
MA	Magnetometer
SP	Self potential
HF	(Conventional) hydraulic fracturing
FHF	Fatigue hydraulic fracturing
HFX	Hydraulic fracturing experiment No. X
F	Initial fracture
RFX	Refracture No. X
MS	Microseismicity
MT	Magnetotelluric
H, E	Magnetic, electric field
P_c	Fracture breakdown pressure
P_r	Fracture reopening pressure
P	Injection pressure
P_p	Packer pressure
Q	Fluid flow rate
V_i	Injected volume
V_r	Recovered volume
S_1, S_2, S_3	Principal stresses (max., intermed., min.)
S_V	Vertical stress
S_H, S_h	Horizontal stress (max., min.)
T_0	Tensile strength
ISIP	Instantaneous shut-in pressure
AG	Ävrö granodiorite
fgDG	Fine grained diorite-gabbro
fgG	Fine grained granite

rock mechanics on-site are well known from a large number of field experiments related to deposition of spent nuclear fuel and radioactive waste. We benefitted, in particular, from the overall knowledge of *in situ* stresses at Äspö from previous HF (Klee & Rummel 2002), overcoring tests (Ask 2003), and integrated stress determination using data from the two methods (Ask 2006).

Klee & Rummel (2002) performed HF stress measurements in one horizontal (level 450 m) and one vertical borehole (measuring section 456 m). According to their results, the maximum horizontal compressive stress (S_H) is the largest principal stress (S_1) with magnitude of 22 MPa and has an orientation of 120° with respect to magnetic north. At this depth level, the vertical stress (S_V) and the minimum horizontal stress magnitude (S_h) are similar ($S_2 = S_V =$ 12 MPa and $S_3 = S_h = 11$ MPa).

For convenience in Table 1, the symbols and abbreviations used throughout this study are summarized.

2 EXPERIMENTAL SETUP AND FLUID INJECTION SCHEMES

Strictly speaking, testing the FHF concept requires determining the fracture breakdown pressure (P_c), detecting the seismic activity with fracture growth, and validating the permeability enhancement process. Therefore, single-flow rate fracture breakdown tests with continuous water injection and multiple-flow rate fracture breakdown tests with alternative injection schemes were tested in the field under controlled conditions. Alternative injection schemes applied to pressurize the fracture tip in a cyclic way (FHF concept, Zang *et al.* 2013) are realized by multiple-flow rate fracture breakdown test. Technically, these tests require changing the flow rate several times before the fracture breakdown occurs. This is in contrast to conventional HF where a constant flow rate is used until the fracture breakdown pressure occurs (Fig. 2). In the first alternative injection scheme (called progressive), frequent phases of pressurization and

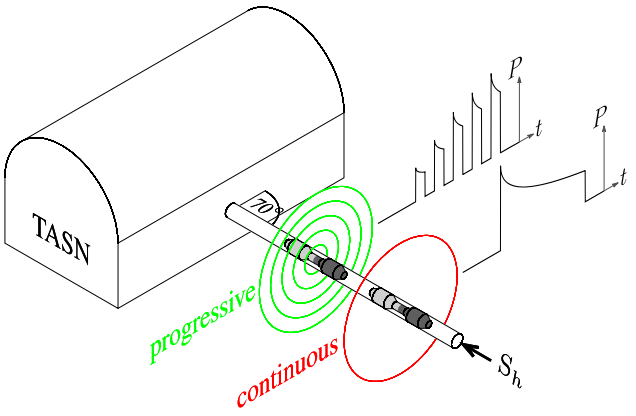

Figure 2. Basic idea of the hydraulic *in situ* experiment. At depth level 410 m, hydraulic fracturing is performed in a subhorizontal borehole (diameter 4 inch) drilled from the experimental tunnel TASN in Äspö HRL. Fractures are generated by different water injection schemes. Schematically, the conventional, single flow rate fracture breakdown test with continuous increase of pressure versus time curve is shown (continuous injection), and compared to the multiple-flow rate fracture breakdown test with five pressurization bands and progressive increase of target pressure interrupted by four depressurization bands before the fracture breakdown occurs (progressive injection). The hydraulic fracture initiation and growth process is mapped by extensive AE, MS and EM sensor arrays, simultaneously.

depressurization are generated in the testing interval while the target pressure is increasing until the breakdown pressure is reached (Fig. 2). The second alternative injection style to change the pressure at the fracture tip frequently is called dynamic pulse injection. Technically, this operation includes a pressure pulsing device (hydraulic hammer) which is described in detail in Section 2.3.1. Three monitoring arrays (AE, MS and EM) in the near field and far field of the fracture nucleus are operated simultaneously to obtain information on hydraulic fracture initiation and growth from three different fluid-injection scenarios (namely continuous-, progressive- and pulse injection). The general setup of the experiment consists of a horizontal borehole drilled from tunnel TASN with two hydraulic testing intervals (Fig. 2, packered sections) and schematic pressure-time rock response curves, one for conventional, continuous fluid injection (Fig. 2, continuous), and one for progressive-water injection (Fig. 2, progressive).

The stress conditions from Klee & Rummel (2002) were assumed to be valid, that is, if the borehole is drilled in the orientation of S_h, such stress conditions would favour the propagation of radial and parallel fractures (Fig. 2). The three-dimensional stress state at the site is discussed later further in detail with the layout of AE monitoring. In the existing experimental tunnel TASN of Äspö HRL, a subhorizontal borehole was drilled with 4 inch (102 mm) diameter in the direction of S_h. The borehole is drilled to approximately 30 m length covering several sections for the testing procedure. A high resolution borehole camera, scanning the entire borehole, and the drill cores were used to select suitable test sections. In phase I of the experiment, a conventional fracture test with continuous increase of fluid pressure in the testing interval is carried out. For this, a single-flow rate test is used until the fracture breakdown pressure P_c is reached. After the hydraulic fracture is generated the flow in the injected part of the borehole is determined with a Lugeon test (Singhal & Gupta 1999). Following the flow test an impression packer is used to map the fracture orientation. In phase II, the hydraulic test is modified and a different water injection style is used (i.e. progressive) with frequent stages of depressurization and

progressively increasing target pressure before the fracture breakdown pressure is reached. This allows stress relaxation at the fracture tip. After the multiple-flow rate test, an impression packer is used to map fracture orientation from the progressive water injection test. Phases I and II of the experiment are repeated in different rock formations, and are operated with fracturing equipment of two different companies.

2.1 Rock mass at test site

The island of Äspö and surrounding areas belong to the Transscandinavian Igneous Belt (TIB) of the Svecofennian Orogen which forms the core of the Fennoscandian Shield in Sweden and Finland. The bedrock in TIB is dominated by well preserved, approximately 1.8 Ga old intrusive rocks varying in composition between granite, syenite, diorite and gabbro. The most prominent ductile structure at Äspö intersects the island in an NE–SW direction (deformation zone NE2). Subsequently, the rock mass is subjected to repeated phases of brittle deformations under varying regional stress regimes and followed by reactivation along earlier generated structures. With few exceptions the deformation zones in Äspö HRL are of brittle type, and are complex and involve series of reactivation events. The complexity of the fracture system at the test site is illustrated by the presented drill cores from the centre part of the hydraulic testing borehole F1 and selected borehole images of F1 (Fig. 3).

Borehole images are obtained by a borehole camera observation tool called BIPS (Döse *et al.* 2008). Four different rock types are found along borehole F1. Close to the tunnel TASN (section 0–6 m) the testing borehole consists of Äspö diorite and fine grained granite (fgG) followed by (7–17 m) fine grained diorite-gabbro (fgDG) and to the end of the borehole (18–28 m) of Ävrö granodiorite (AG). Fig. 3 shows some of the geology along the borehole in the range 24–26 m and the fractures intersecting drill cores. The average fracture frequency of the 86 mm diameter drill core is four fractures per metre. Test sections for HF are selected based on information from borehole images (Fig. 3a) and core sections without fractures (Fig. 3b). For convenience, the hydraulic test interval of experiment HF1 described in detail later, is marked in Fig. 3 by red rectangles.

2.2 Selection and orientation of drill holes

The test site selected is located in the Äspö extension area 2011–2012, at depth level of 410 m below surface. Based on the geological and hydrological description of this area (Stenberg 2015), a monitoring design with borehole location and geometry has been developed. In Fig. 4, an overview of the test site and the surrounding area is given. The location of the experimental tunnel TASN is seen from which four long boreholes were drilled (Fig. 4a, thin black lines). The middle borehole (Fig. 4a, F1) serves as HF borehole and was drilled to a total length of 28.40 m subparallel to the orientation of the minimum horizontal compressive stress, down dipping -4°. The monitoring boreholes (Fig. 4a, M1-M3) were drilled with inclination upwards. Owing to the presence of a hydrological conductor producing up to 75 mL s^{-1} outflow of water, sensor installation was possible only in upward oriented boreholes.

The orientation of boreholes M1, M2 and M3 were chosen in order to maximize the coverage of expected seismic activity with AE and accelerometer sensors, while to the same time not to disturb the rock volume of HF. In this sense, we secured the hypocentres of possible seismic events with optimally surrounded sensors taken into account the tunnel geometry and source receiver distances.

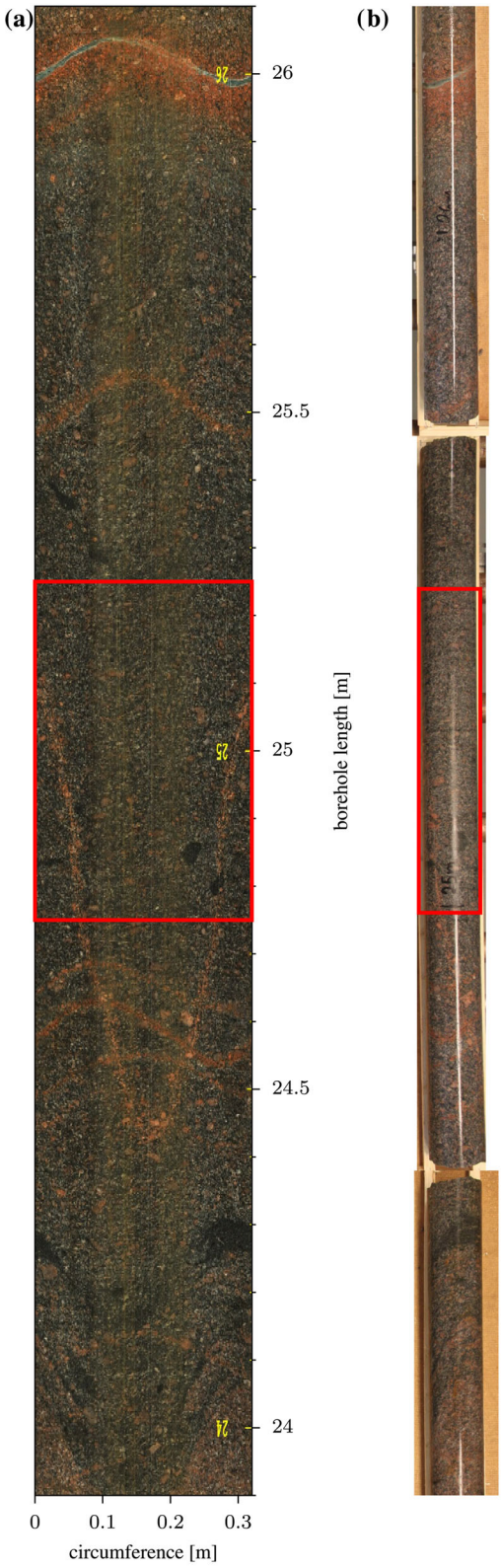

Figure 3. Complexity of naturally fractured rock mass at Äspö HRL with selected test interval of experiment HF1 in Ävrö granodiorite (AG) marked by red rectangles. (a) Borehole images from the BIPS tool in the range of 24–26 m of borehole F1. (b) Composite photo of the drill cores in the same range as the borehole image in (a). The black numbers on the core are approximations of the core length only and the test interval is shown approximately by the red rectangle.

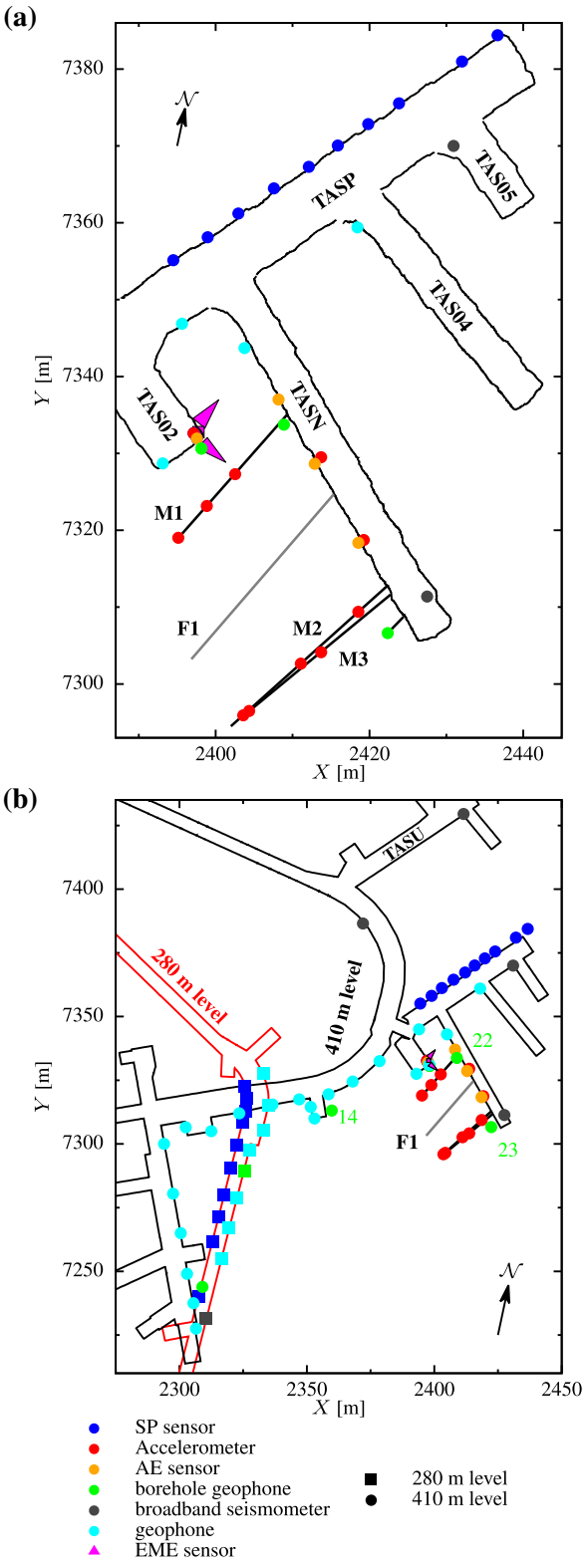

Figure 4. Test site at Äspö HRL (a) in the near field, and (b) in the far field. Hydraulic testing borehole F1 and monitoring boreholes M1, M2 and M3 are drilled from tunnel TASN, subparallel to the minimum horizontal stress direction. Symbols indicate different sensors of the AE, MS, and EM monitoring network (with EME sensors oriented in the direction of the arrows). In (b), sensor colours are identical, and the two depth levels are indicated by different symbols (280 m level–square, 410 m level–dot), except for the EME sensors.

The monitoring borehole northwest of the fracturing borehole F1 (Fig. 4a, M1) has a total length of 22.10 m with inclination +10°. The boreholes southeast of the fracturing borehole F1 are located above each other and were drilled with different inclinations (Fig. 4a, M2 total length 30.10 m with inclination +26°, and M3 total length 24.05 m, inclination +4°). This geometry in the predetermined stress state allows propagating HF perpendicular to borehole F1, in the direction of maximum horizontal compressive stress, and in a direction towards the monitoring boreholes. The four long boreholes (F1, M1-M3), and additional twenty-three short boreholes for inserting MS, EM and additional AE sensors (Fig. 4, symbols along tunnel walls) were started to be drilled and completed in May 2015. A detailed description of all sensors shown in Fig. 4 is given in Section 3.

2.3 Hydraulic fracturing

In this section, the experimental setup and equipment used for continuous water injection and alternative water-injection schemes are described. In the following, the alternative, multiflow rate fracture breakdown tests are separated into progressive water injection and dynamic pulse-injection scenarios. MeSy Solexperts, Bochum (Germany) performed the progressive test, and ISATech s.r.o., Prague (Czech Republic) performed the dynamic pulse test. In addition, each company performed two conventional HF tests.

2.3.1 Hydraulic fracturing equipment

MeSy Solexperts performed two conventional HF and one multiflow rate test with five bands of pressurization and four bands of depressurization with increasing target pressure before the fracture breakdown occurred (progressive water injection scenario). MeSy Solexperts was using the straddle packer assembly Perfrac-II equipped with steel reinforced packer elements IPI with 92 mm outer diameter (OD). The sealing length of each packer element is about 1.0 m and the test interval was reduced from 0.7 to 0.5 m. All three tests by MeSy Solexperts (HF1, HF2 and HF3) were performed with the test interval of 0.5 m. The straddle packer was moved and fed with a 16 mm OD steel pipe. It was pressurized via high pressure steel coil tubing with maximum operating pressure of 60 MPa. An electric driven pump (SPECK, type HP 400/2-10) with the capacity of 0.17 L s^{-1} and maximum pressure of 40 MPa was used. Interval and packer pressure were measured uphole at the recording unit in tunnel TASN. A sixteen channel sampling system of type Solexperts SCI-A was used as data acquisition system. The orientation of the fractures is determined with an impression packer. The impression packer is oriented with a magnetic single shot orientation tool.

The pulse water injection test was performed by ISATech Prague using WATRAD Ltd. hydro-fracturing equipment with the newly developed hydraulic straddle packer equipment and pump system described by Semíková *et al.* (2014) and Jiráková *et al.* (2015). The equipment consists of a high capacity hydraulic pump that can deliver a linear and dynamic water pressure increase with different amplitude up to 30 MPa and a maximum flow rate of 0.15 L s^{-1}. A hydraulic oil pump delivers the pressure for the pulse device with a maximum working pressure of 20 MPa. The pulse device acts like a hydraulic hammer and generates a pulse simultaneous with the progressive pressurization in the test section. Depending on pressure of nitrogen, oil and water different amplitudes can be generated. The frequency of the pulse can be regulated within the range

Table 2. Overview about the six hydraulic fractures of the *in situ* experiments with start and stop times (in UTC), depth of testing interval, rock type, injection style, and company name performing the test. The fatigue concept is simulated in experiment HF3 (progressive injection) and in experiment HF5 (pulse injection). Hydraulic results include fracture breakdown pressure (P_c), reopening pressure (P_r) and horizontal minimum stress (S_h). S_h is determined from the instantaneous shut-in pressure (ISIP). P_r is measured at the first refrac (RF) of each treatment.

Experiment	Date	Start	Stop	Mid test interval [m]	Rock type	Injection style	P_c [MPa]	P_r [MPa]	S_h [MPa]	Company
HF1	June 3	9:40 13:44	10:17[a] 15:30[a]	25.0	AG	Continuous	13.1	8.9	8.3	MeSy
HF2	June 4	07:15	8:57	22.5	AG	Continuous	10.9	6.7	8.6	MeSy
HF3	June 4	12:07	13:13	19.0	AG	Progressive	9.2	8.8	9.2	MeSy
HF4	June 9	12:29	13:44	13.6	fgDG	Continuous	10.6	9.0	8.5	ISATech
HF5	June 10	12:49	14:02	11.3	fgDG	pulse	9.0[c]	8.6	7.5	ISATech
HF6	June 11 June 12	13:17 07:15	14:10[b] 8:38	4.8	fgG	Continuous	11.3	4.8	8.1	ISATech

[a]Interruption due to impression packer test.
[b]Underground time limit was exceeded, operation resumed next day.
[c]Determined during third cycle.

3–10 Hz. The control panel allows controlling the test manually and the response is recorded with a data recorder. The hydraulic driven straddle packer has four rubber elements that seal off the testing interval of length 0.25 m against the borehole wall by clamping. For this, a hydraulic system shortens each of the hard rubber elements in the axial direction of the packer and the increase of radial dimension generates the clamping towards the borehole wall and seals the test interval of the packer. All three tests by ISATech (HF4, HF5 and HF6) were performed with the test interval of 0.25 m.

2.3.2 *Planning of the operational phase*

During the experimental phase of the project (June 2015), six hydraulic fractures were generated in fracturing borehole F1 in three different rock formations. Analysis of drill cores and BIPS borehole camera images of type optical televiewer (Döse *et al.* 2008) of borehole F1 have been carried out to select appropriate test intervals. Suitable test intervals for HF with good rock conditions, in particular rock free of visible, pre-existing fractures have been selected from core and borehole images. One example of selecting the test section of HF1 is shown in Fig. 3. In Table 2, specific data for six hydraulic fractures generated (experiments HF1–HF6) are listed. Data include the actual day of testing with start and stop times, the borehole length at mid-test interval, the rock type, the water injection style, and the name of company performing the test.

In Table 2, three columns are added with results from hydraulic testing (P_c, P_r, S_h) to be discussed in Section 4. In the deeper section of borehole F1, MeSy Solexperts carried out the tests HF1 (continuous water injection), HF2 (continuous water injection) and HF3 (progressive water injection) in the AG at 25.0, 22.5 and 19.0 m borehole length, respectively. In the shallower section of the fracturing borehole F1, ISATech operated tests HF4, HF5 and HF6. Two tests, HF4 (continuous water injection) and HF5 (pulse water injection), were performed in the fgDG at borehole length 13.6 m and 11.3 m, respectively. The last test HF6 (continuous water injection) was carried out in fgG located closest (4.8 m) to the tunnel surface. Note that the depth of the excavation damaged zone from drilling and blasting extends up to 1.3 m into the floor of the tunnel and 0.8 m into the roof, but very limited distance into the sidewalls (Emsley *et al.* 1997).

2.3.3 *Hydraulic test procedures*

The *in situ* HF tests were carried out between 2015 June 3 and 12 (Table 2). The test procedure for conventional HF tests follow the International Society of Rock Mechanics (ISRM) suggested method for HF stress measurements (Haimson & Cornet 2003) and is described by Zang & Stephansson (2010). The typical test starts with the inflation of the packer system to seal the interval, followed by a rapid pressurization with water to test the system for potential leakage (pulse integrity test). During the subsequent main test phase a constant injection rate is applied. Pressure increases until it reaches the fracture breakdown pressure (P_c), followed by a decline to a stable pressure level called the fracture propagation pressure. After stable pressure conditions are reached, the well is shut-in and the pressure drops rapidly to the instantaneous shut-in pressure (ISIP) followed by a decline curve. The ISIP is assumed to be equivalent to the minimum principal stress S_3. Finally, the interval pressure is released and the fluid volume is recovered. The test procedure is repeated several times to obtain the fracture reopening pressure P_r at each test cycle.

The tensile strength of rock, T_0, is calculated from the difference of P_c and P_r (Haimson & Cornet 2003). It is assumed that the fracture has been closed completely in between the cycles. This implies that no shearing has been involved that potentially results in a residual opening of the fracture walls.

The test procedure for the progressive water injection consists of a modified pressure scheme. First the pressure is increased to 20 per cent of the fracture breakdown pressure obtained from the conventional test in the same formation. Then, a shut-in for several minutes follows with subsequent pressure release (depressurization phase). Thereafter, the pressure is increased by a level approximately 10 per cent above the previous pressure level following the same scheme (progressively increasing target pressure). After shut-in another depressurization phase follows. The pressurization and depressurization sequences are repeated until a pressure drop occur indicating rock failure, that is, the start of the fracturing process. The subsequent refracturing tests follow the same scheme like the repetitions of the conventional test procedure. Therefore, the treatments are different for pressures below the breakdown pressure only, that is, single-flow rate versus multiple-flow rate fracture breakdown tests.

The pulse HF test (Jiráková *et al.* 2015) is a modification of the progressive injection test. The hydraulic equipment for the pulse dynamic test consists of a hydraulic pump to maintain linear and dynamic pressure levels (pressurization bands) together with an additional hydraulic pressure pump to drive the dynamic pulse tool with adjustable amplitude and frequency (5–6 Hz in experiment HF5). Both pressure signals are combined to result in dynamic pressure pulses overriding different predefined pressure levels.

3 MONITORING NETWORKS

All phases of the HF *in situ* experiment were monitored with three passive systems, that is, AE, MS, and EM sensors. Whereas MS sensors recorded seismic waves with frequencies up to 1 kHz, *in situ* AE sensors recorded smaller seismic events with frequencies up to 100 kHz. For the purpose of this paper, we call seismic events recorded with AE and MS sensors AE and MS events, respectively. Tests are designed (1) to locate and trace AE events, MS events in space and time and EM events in time, (2) to identify individual crack mechanisms and (3) to investigate crack interaction in the nucleation and growth process of hydraulic fractures in naturally fractured rock mass. During a total of twenty-nine fracturing stages, the three monitoring systems were up and running to document multiple fracture wall opening and closing operations. In total, thirty-nine sensors were operated in the near field (at depth level 410 m, Figs 4a and b) close to the testing borehole. Thirty-six sensors were deployed in the far field above (depth level 280 m and at the surface) and below (depth level 450 m) the fracture initiation point. MS systems operated combined in the near and far field. The AE monitoring system was operated by Gesellschaft für Materialprüfung und Geophysik (GMuG) mbH, Bad Nauheim (Germany). This network was designed to monitor in the frequency range from 1 to 100 kHz (accelerometers from 50 Hz to 25 kHz, AE sensors from 1 to 100 kHz). The German Research Centre for Geosciences (GFZ) operated an MS array with geophones (4.5 Hz to 1 kHz), borehole geophones (28 Hz to 1 kHz) and broad-band seismometers (flat velocity response from 1/120 to 100 Hz) operating in both, the near and far field. The Karlsruhe Institute of Technology (KIT), Germany operated a third system to detect EM signals from hydraulic fracture growth. The EM array involved surface monitoring with one full MT station, and underground monitoring of electromagnetic emission (EME), self-potential (SP) and broad-band magnetometers (MA) in three directions with borehole sensors. Underground, the sensors were placed at three different depth levels (450 m, 410 m and 280 m). EME, MT/MA and SP during rupture process were detected at different frequencies from 37 to 50 kHz, at 512 Hz and at 1 Hz, respectively.

The AE monitoring system was synchronized to the MS system by the simultaneous recording of one geophone on both systems. MT and magnetic stations were synchronized by internal GPS. EME and SP were synchronized with external GPS time.

3.1 Acoustic emission monitoring network

The *in situ* AE monitoring network consists of eleven AE sensors (GMuG MA BLw-7-70-75) and four accelerometers (Wilcoxon 736T). AE sensors employed are uniaxial side view sensors for borehole installation (Fig. 4a, red dots). The sensors were developed by GMuG for *in situ* AE monitoring, that is, very sensitive recording in the frequency range of 1–100 kHz (Philipp *et al.* 2015). They are capable to monitor fractures from centimetre to metre scale (Kwiatek *et al.* 2011). AE sensors are operated with 1 kHz analogue high-pass filter. The AE sensor does not have a flat sensor response, but displays weak resonance frequencies that improve the sensitivity of the recording. The employed accelerometers have a flat (± 3 dB) frequency response between 2 Hz and 20 kHz. Accelerometers are operated with an analogue 50 Hz high-pass filter (Fig. 4a, orange dots). The dynamic range is 100 mV g^{-1}. All sensors are installed inside boreholes. Eight AE sensors are installed in the long monitoring boreholes M1-M3, surrounding the fracturing borehole F1. The remaining sensors are installed in short boreholes near the roof of tunnels TASN and TAS02 (Fig. 4a).

Data was recorded using the measuring system GMuG AE-System that is suitable both for continuous recording of data and recording in trigger mode. The *in situ* AE monitoring network was operating in trigger mode from 2015 June 3 to 22 recording waveform windows of 32.768 ms for all triggers. A second acquisition system recorded in parallel the continuous full waveforms from all channels during all HF time periods. Both trigger and continuous recording systems were performed with 1 MHz sampling rate. Recording in trigger mode allows for (near) real time assessment of AE events using automatic event detection and localization based on automatic *P*- and *S*-wave onset picking. The sixteen-channel transient recorder was operated with a ± 10 V input range. In trigger mode the recording and validation unit gets activated once an operator set threshold is exceeded. In this experiment very sensitive trigger conditions were chosen *in situ* to maximize the sensitivity of the network. Once a trigger is detected, data is recorded on all synchronized channels. A ring buffer for pre-trigger recording is implemented. Picking of *P*- and *S*-wave onsets is based on a Hilbert transform and a modified short time average/long time average (STA/LTA) algorithm (Allen 1978, 1982). Localization is based on gradient descent and a modified least squares algorithm.

For localized events the AE magnitude is estimated. The AE magnitude is a relative magnitude after Eisenblätter & Spies (2000) and is not comparable with common seismological magnitude scales. The AE magnitude gives a rough estimate on the event size. The AE magnitude is calculated as

$$M_{\mathrm{AE}} = 20 \log_{10} A \quad \text{with} \quad A = \frac{A_0 r}{r_0} e^{\alpha (r - r_0)}.$$

A_0 corresponds to the *P*-wave amplitude, normalized to 1 μV signal amplitude at signal output. The amplitude is measured at a frequency of 7.5 kHz. Parameter r corresponds to the source receiver distance. The scaling parameter r_0 is approximately equal to the average of all source receiver distances. Here $r_0 = 20$ m was chosen. The exponent α represents the damping and was set to 0.02 m^{-1}.

Velocities for both *P*- and *S*-waves were obtained from active ultrasonic transmission tests. For this an ultrasonic pulse transmitter was inserted in fracture borehole F1 before the experiment. Active pulses were sent from one-metre intervals and recorded at the sensors of the AE network. Based on traveltime analysis averaged velocities were obtained. The retrieved velocity values are 5810 ± 120 m s^{-1} and 3400 ± 200 m s^{-1} for *P*-wave and *S*-wave, respectively. For localization of AE events a homogeneous, full space velocity model was used with $v_p = 5800$ m s^{-1} and $v_s = 3200$ m s^{-1}.

3.2 Seismic monitoring network

The installed seismic stations are sensitive in the frequency range from approximately 4 Hz to some 100 Hz. At 19 locations along the 410 m depth level (Fig. 4b, cyan dots) and at seven positions at the 280 m depth level (Fig. 4b, cyan squares), PE-6/B geophones (SENSOR SM-6 4.5 Hz U-B and H-B, Nederland) were installed. Based on previous experience (Picozzi *et al.* 2010b; Oth & Picozzi 2012), the standard steel spikes are removed and the geophones were fixed to an adjustable aluminium bracket with two supporting bars for minimizing spurious vibrations. The bracket is fixed to the wall and the geophones were connected in a horizontal position, with the north component oriented towards the tunnel wall and the east component parallel to the tunnel wall. Three-component borehole

GS14-L3 geophones (Krauß *et al.* 2014) with a frequency range from 28 Hz to 1 kHz were installed in 1 and 3 m long, horizontal boreholes; five geophones at the 410 m depth level and one at the 210 m depth level (Fig. 4b, green dots/squares).

We used three twenty-four channel recorders (Geode, Geometrics) connected by an interface cable using TCP/IP and an interface box to a PC LAN socket. Twenty-four three-component geophones were connected at 410 m depth level and eight three-component geophones were connected at the 280 m depth level. Data were streamed to the recorder box, and then transmitted to the PC hard drive for display and event detection. Continuous data were recorded for two weeks, with a sample rate of 1 kHz during the hydraulic testing times listed in Table 2. During nights and weekends, the sample rate was reduced to 250 and 125 Hz, respectively. Charging of the batteries used for Geode's power supply was conducted continuously except for the HF1–HF6 test time windows (Table 2), in order to minimize electrical interference.

For the identification of low frequency signals, five broad-band seismometers (Trillium Compact 120s, Nanometrics) were installed at different hard rock sites (Fig. 4b, grey dots/square). In other experiments, tiltmeters are used to detect displacement gradients in 2-D, that is, horizontal tilt (Sleefe *et al.* 1995; Jeffrey *et al.* 2009; Dahi Taleghani & Lorenzo 2011; van der Baan *et al.* 2013). In our installation the broad-band seismic sensors were sensitive to displacement velocities in three dimensions and to horizontal. Four broad-band sensors were located at depth level 410 m near the HF experiment (Fig. 4b, grey dots) and one broad-band sensor was placed at depth 280 m (Fig. 4b, grey square). The seismic signals were digitized and stored by 24 bit stand-alone three-channel digital recorders (CUBE, Omnirecs), which were synchronized by built-in GPS every few days. A pre-amplifier gain of 1 was chosen and the sample rate was set to 200 Hz. No indoor GPS system was available. For the synchronization of underground stations four additional CUBE recorder are used which were set to 800 Hz to record seismic ground motion parallel to the Geode system.

The installed MS system at 410 m depth level allows for the detection of very small seismic events with moment magnitudes below −2 (e.g. Picozzi *et al.* 2010a; Goertz *et al.* 2012) because the maximum distance of sensors to the fracturing borehole F1 at depth level 410 m is approximately 100 m, and the maximum distance of sensors to the fracturing borehole F1 at depth level 280 m is approximately 150 m, respectively. As mentioned in the introduction, such seismic events (magnitude range −4 to −2) are called picoseismicity. However, the two limiting factors for detecting picoseismic events in Äspö HRL appears to be (1) the 50 Hz electrical underground installation (and its overtones), and (2) the acoustic noise from the air ventilation system and operating machinery.

3.3 Electromagnetic monitoring network

The EM monitoring network with its EME, SP and MT/MA sensors was operated at frequencies between 1 Hz and 50 kHz. EME are measured using a beam antenna/ferrite aerial (300 mm long) with a receiver covering a frequency range between 5 and 50 kHz (Cerescope) (Hagag & Obermeyer 2016). The antenna is most sensitive to the *H*-component of the EM field. The maximum amplitude of the signal is expected to be parallel to the hydraulic fracture plane. The amplification of the instrument ranges between 90 and 120 dB, that is, a sensitivity of 5 $\mu A\,m^{-1}$. In the case of HF1, we used a frequency range of 37–50 kHz. The discrimination level is set to separate the geogenic signal from the background noise. Four different parameters (*A*–*D*) are recorded: *A*, the number of peaks, *B*, the number of pulse packages, *C*, the average amplitude of the pulse packages, and *D*, the related energies. For each 1 s time interval, data are measured over a 0.1 s time window, using a sampling frequency of 100 kHz. Two sensors were installed in 0.45 m long boreholes drilled with a bearing of 40°and 130° (Fig. 4a, magenta triangles in TAS02 (EME)). The sensors are expected to be perpendicular and parallel to the fracture plane at distances between 15 m and 25 m from the different mid test intervals (e.g. approximately 25 m from experiment HF1). A third, vertically oriented sensor failed to operate during testing on-site.

Self-potential (SP) measurements were acquired at a sampling frequency of 1 Hz using two electrode chains with $Pb/PbCl_2$ PMS9000 non-polarizable electrodes (SDEC, France) filled with NaCl saturated solution. The near field electrode chain (Figs 4a and b; blue dots) was set to a distance between 50 and 75 m from the different experiments (about 25 m from experiment HF1) and the electrode offset was 5–10 m at the 410 m level. The far field electrode chain (Fig. 4b, blue squares) was installed at a distance of approximately 150–200 m with electrode offsets between 5 and 20 m at the 280 m level. The electrodes were fixed and coupled to the massive granite in 0.25 m long boreholes using bentonite. The northeasternmost electrodes of the two chains were used as ground for all dipoles. Data were recorded typically in 24 hr windows using a CR-6 (Campbell Scientific) with an input resistance of 20 GΩ.

MT measurement setup includes two distant stations, equipped with Metronix MFS07e soft coils magnetic sensors and ADU-07 data loggers. The time series of magnetic (*H*) and at the surface electrical (*E*) components were recorded quasi-continuously (in 86 340 s packages) at 512 Hz. The MA station TASS (located at about 500 m distance from HF1 to the East) comprises of three magnetic sensors that were oriented approximately parallel (azimuth 308°, vertical, X- and Z-components respectively) and perpendicular (azimuth 38°, Y-component) with respect to the expected fracture plane. At the surface MT station (57°26′10.03″N, 16°39′10.66″E), two magnetic sensors and non-polarizable $Pb/PbCl_2$ electrode pairs with 100 m offset were oriented to the north and east. A vertical magnetic sensor was in-stalled above the surface due to impenetrable granitic subsurface. Permanent remote reference data from the Wittstock station in Germany (Eydam & Muñoz 2011) is available for data processing.

4 RESULTS

This section consists of four parts. After discussing the hydraulic response of rock mass, the results of the three monitoring networks follow.

4.1 Hydraulic response of tested rock mass

Results from six hydraulic tests are listed in Table 2. The fracture breakdown pressure P_c is determined from initial fracturing cycle of conventional HF. The fracture reopening pressure P_r is determined from the first refrac cycle of HF (RF1). The magnitude of the minimum horizontal stress S_h is determined from the instantaneous shut-in pressure ISIP. The vertical stress $S_V = 10.9$ MPa is computed from rock density $\rho = 2720\,kg\,m^{-3}$ and the depth level of the borehole (406.8 m).

Representative examples of each injection style are provided in Figs 5 and 6. This includes the single-flow rate experiment with conventional, continuous injection (Fig. 5a, HF2), and two

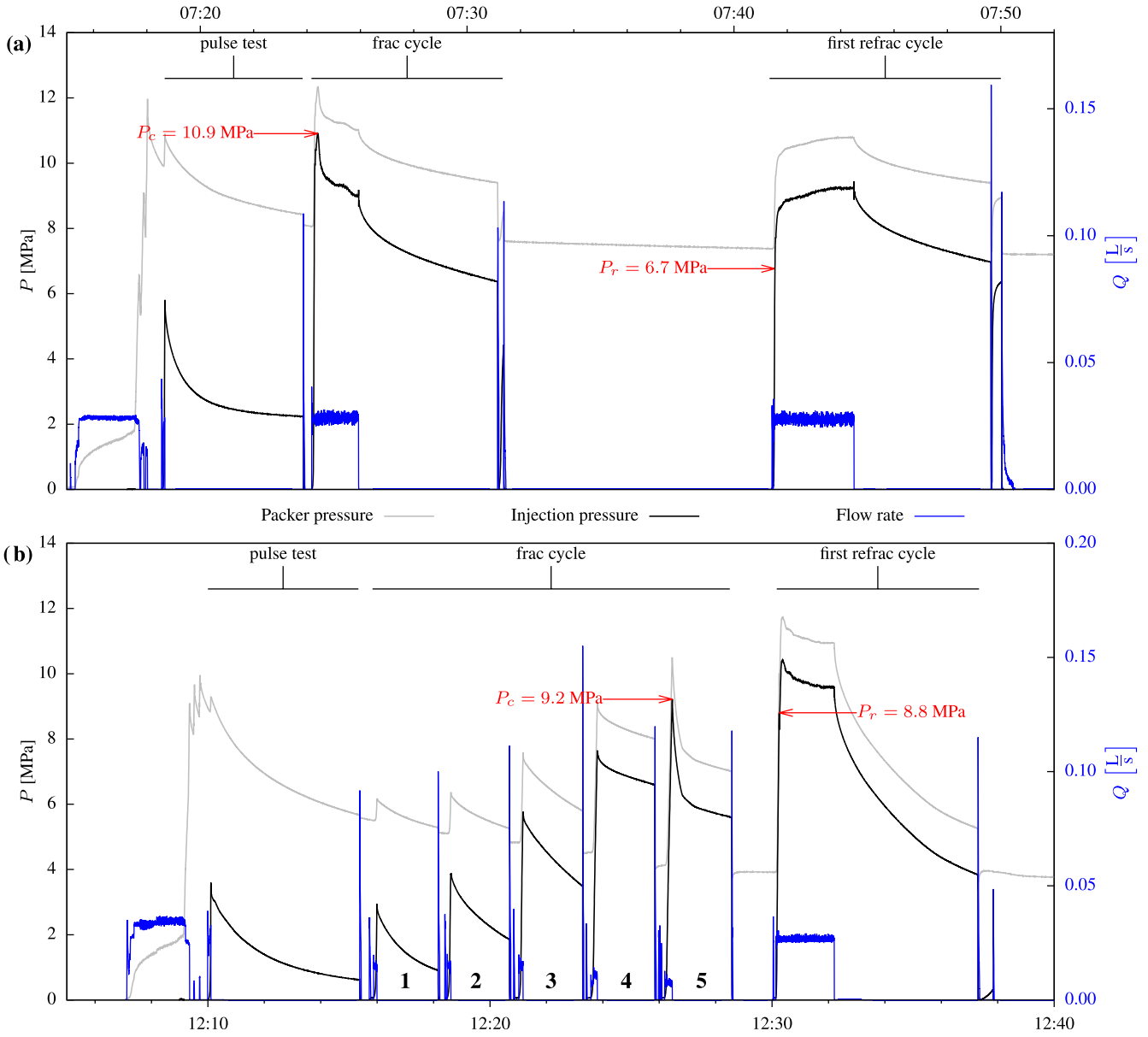

Figure 5. Comparison of conventional HF with continuous water injection and alternative testing with progressively increasing target pressure interrupted by four depressurization phases. Interval pressure (black curve), packer pressure (grey) and flow rate (blue curve) are plotted versus time. (a) Experiment HF2 with continuous injection at 22.5 m depth of borehole F1. Following the pulse test, the initial frac cycle and the first refrac cycle are shown. (b) Experiment HF3 with progressive water injection at 19.0 m depth of borehole F1. After the pulse test, the fatigue procedure is manifested in five bands of stepwise increasing target pressure interrupted with four intervals of depressurization, followed by the first refrac cycle analogue to the conventional test.

multiple-flow experiments with progressive water injection (Fig. 5b, HF3) and dynamic pulse injection (Fig. 6, HF5). In Fig. 5, there is a 2 L s^{-1} flow rate injection lasting for about 2 min at the beginning of both tests. This is an integrity test (pulse test) with rapid pressurization of the test interval to a differential pressure of about 1 to 3 MPa and subsequent monitoring of the pressure decline for approximately 10 min. For convenience, also the packer pressure is included in Fig. 5 together with the interval pressure and the flow rate. The initial fracturing cycle (HF2-F) and first refrac of HF2 (HF2-RF1) at 22.5 m borehole length indicate $P_c = 10.9$ MPa and $P_r = 6.7$ MPa for the AG formation (Fig. 5a). In Fig. 5b, the result of the progressive water injection test (experiment HF3) at 19.0 m borehole length are documented. The interval pressure (Fig. 5b, black curve) is increased to about 20 per cent of the P_c from the conventional HF2 test for a duration of 8 s, followed by a shut-in for 130 s and a bleed-off for 3 s. The subsequent depressurization phase lasted for about 10 s. Afterwards, the interval pressure is increased at each step by about 10 per cent with respect to the previous pressure level following the same procedure. After five bands of progressively increasing target pressure (numbered in Fig. 5b) interrupted by four bands of depressurization (up to half minute duration), the breakdown pressure is determined to be 9.2 MPa. This value is 15 per cent lower compared to the value of P_c from the conventional HF2 experiment, and 30 per cent lower compared

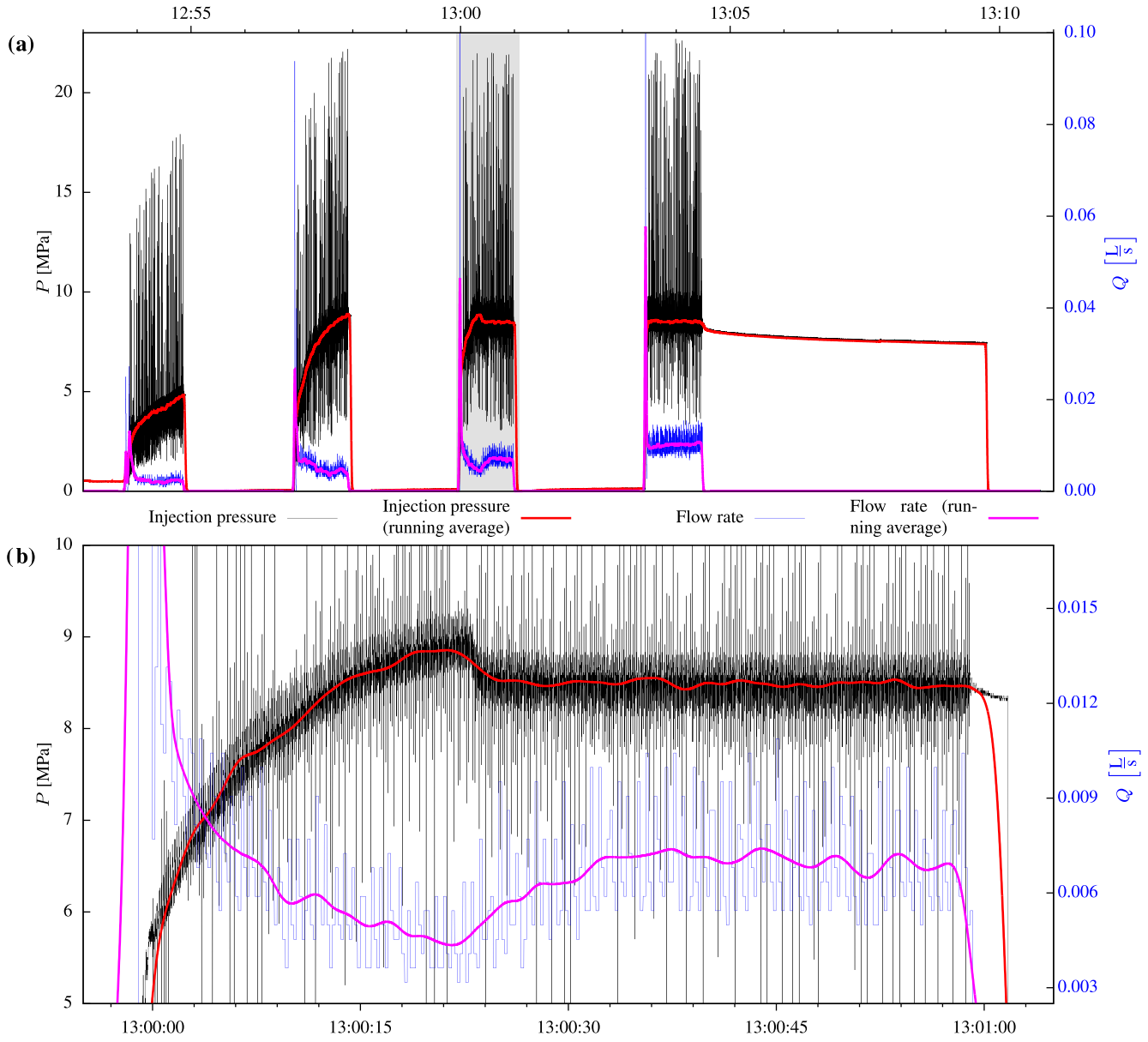

Figure 6. Pulse injection test in borehole F1 at depth of 11.3 m. Dynamic water pulsing with a frequency of approximately 5 Hz is performed. (a) Overview chart of pulse experiment HF5. The breakdown pressure P_c is estimated from the running average of the interval pressure during the third cycle. (b) Detailed view of the third pressurization band of experiment HF5. The running average of the pressure indicates a pressure decrease after reaching 9 MPa with a simultaneous increase of the flow rate.

to the value of P_c from the first conventional HF1 experiment in the same rock type (see Table 2). Note that only the absolute value of flow rate is shown in Fig. 5 (right ordinate).

Experiment HF5 was performed at 11.3 m borehole length as dynamic pulse test (Fig. 6). For this, pressurizing bands were set to internal pressure values of 2, 4, 6, and 8 MPa, respectively. During the first pressurization band the interval pressure increases from 2 to 4 MPa, for the second band from 4 to 8.8 MPa, and for the third pressurization band from 6 to 8.6 MPa. During the fourth pressurization band with 8 MPa no gradual increase of pressure was recorded indicating the generation of a new fracture at the previous pressurization level. Therefore, P_c of experiment HF5 was determined in the third pressurization band where a clear pressure drop is observed, indicating the breakdown pressure of rock (Fig. 6, $P_c = 9.0$ MPa). Compared to experiment HF4 in the same rock type (fgDG) with continuous water injection at 13.6 m borehole length and $P_c = 10.6$ MPa (Table 2), the fracture breakdown pressure was reduced by 15 per cent using the dynamic pulse treatment instead of the conventional treatment.

The hydraulic tensile strength of the rock formation is calculated from the conventional HF tests. The assumption to achieve a reliable value is a purely tensile fracturing process including the closure of the fracture walls before the subsequent refracturing tests. This is assumed to be the case for the first experiment HF1. The P_r is determined to 8.9 MPa; hence the calculated hydraulic tensile strength of the rock formation is $T_0 = 4.2$ MPa.

To obtain the magnitudes of the stress field it is assumed that the vertical stress is a principal stress. Taking a mean rock density of

2720 kg m^{-3} and the depth of the horizontal well of 406.8 m below surface, the calculation of the vertical stress leads to 10.9 MPa. The minimum principle stress for each experiment is calculated from ISIP (instantaneous shut-in pressure). The mean value of the minimum horizontal stress S_h from all measurements is 8.4 MPa (Table 2).

Based on about 100 HF and 140 overcoring stress measurements in Äspö HRL, Ask (2003, 2006) developed the Integrated Stress Determination Method for the two methods and presented the results for different depths. For the area closest to the test site SE of fracture zone NE-2 Ask (2006, his fig. 9C) found from HF solutions at level 330 m ($S_1 = 20.9$ MPa at 336°/0°, $S_2 = 8.7$ MPa arbitrary/90° and $S_3 = 6.7$ MPa at 246°/0°) and from overcoring stress solutions at level 380 m ($S_1 = 22.6$ MPa at 312°/3°, $S_2 = 9.5$ MPa at 43°/9° and $S_3 = 8.1$ MPa at 200°/80°; see Fig. 10). Stress data will be discussed in the next section together with AE monitoring results.

4.2 *In situ* AE monitoring results

The AE monitoring network successfully recorded and localized AE events during the experiment. Continuous waveforms with 1 MHz sampling were gained during all phases of the experiment. *In situ* triggered AE data were used to obtain first order information about the fracture growth, its location, orientation and extension in near real time. During the experiment all events that were located automatically during fracturing, shut-in or bleed-off were then manually reviewed and plotted on-site. Manual review of picks was necessary because of omnipresent 10 ms electrical pulses introduced false triggers of the first *P*-wave pulse arrivals. For experiments HF1 (continuous), HF2 (continuous), HF3 (progressive water injection) and HF6 (continuous) information on the generated fractures (location, orientation, extension) was gained from the AE event distribution. No information was gained for HF4 (continuous) and HF5 (dynamic pulse injection), because not enough seismic energy was radiated in fine grained diorite gabbro. Information provided *in situ* on the fracture evolution based on localized AE events was used by the project management in the decision making process.

Overall 69 400 triggers were detected *in situ* with trigger mode recordings. Most recorded triggers correspond to transient noise of anthropogenic, electrical or hydrological origin, because of the sensitive trigger conditions. Some recorded events that correspond to noise sources were located, for example working noise generated at the fracturing borehole before or after fracturing experiments (e.g. when the packer is inserted or removed). The waveform signature of most noise events differ clearly from seismic events. Typical waveforms of noise in the kHz range from a South African mine are shown in Plenkers *et al.* (2010). Typical waveforms for seismic AE events recorded during the HF1 experiment are shown in Fig. 7. Eleven waveforms from AE sensor recordings (AE01–AE11) and four waveforms from accelerometer recordings (ACC13–ACC16) are shown for the first event occurring during refrac1 in experiment HF1 (HF1-RF1). During post-processing a seismic catalogue was created that is free of noise events (Appendix A).

During post-processing, events recorded 2015 June 3 9:35AM to 2015 June 15 12:00AM were relocated using optimized automatic picking and localization parameters that suit the nature of AE events recorded *in situ*, that is, more precise filter settings as well as STA/LTA trigger algorithm parameters. The maximum location residual was lowered from 0.8 to 0.3 m and the single location error per station was lowered from 0.8 to 0.5 m in order to improve the location certainty. To exclude noises all waveforms

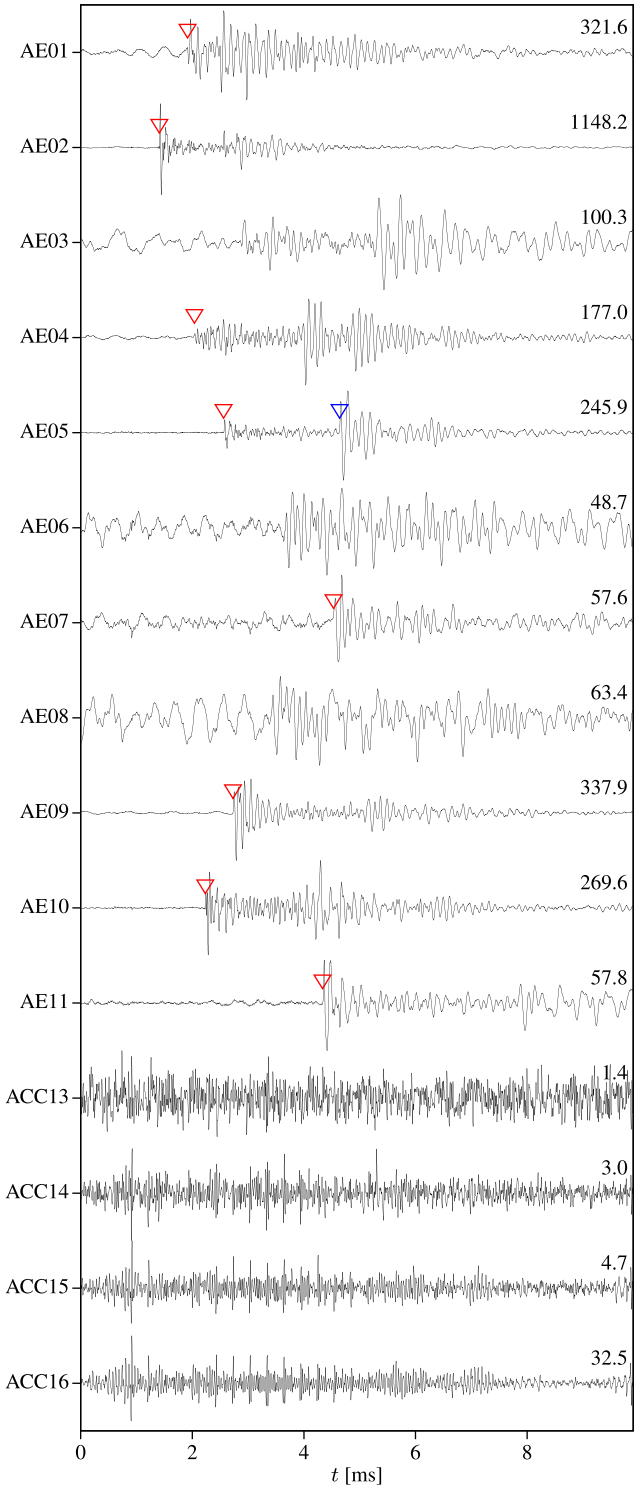

Figure 7. Typical waveform of seismic AE event. The waveform of the first event during hydraulic fracture HF1 is shown that occurred 2015 June 3 at 10:04:07. Waveforms are bandpass filtered (500 Hz to 50 kHz). Picks are shown as triangles (*P*-wave, red; *S*-wave, blue). The amplitude is normalized. True maximum amplitude is given on the right side in mV (AE, AE sensor; ACC, accelerometer).

Table 3. Overview about the 29 stages of hydraulic fracturing at the test site. Six hydraulic fractures were propagated in multiple refracturing phases. Comparison of rock type, fracture breakdown pressure (P_c), fracture reopening pressure (P_r) and additional hydraulic test parameters (Q, water flow rate; V_i, injected volume; V_r, recovered volume) and AE *in situ* relocalized event numbers.

Stage No.	Experiment	Rock type	P_c or P_r (MPa)	Q (L s^{-1})	V_i (L)	V_r (L)	Number of AE, relocated
1	HF1-F		13.1	0.015	0.8	0.5	0
2	HF1-RF1		8.9	0.022	2.7	1.5	3
3	HF1-RF2	AG	7.7	0.027	4.5	1.7	10
4	HF1-RF3		8.6	0.042	5.2	1.9	12
5	HF1-RF4		8.8	0.077	4.7	2.3	4
6	HF1-RF5		8.2	0.078	9.3	5.5	20
7	HF2-F		10.9	0.028	3.8	1.1	8
8	HF2-RF1		6.7	0.028	5.0	1.9	6
9	HF2-RF2	AG	7.5	0.042	1.2	0.6	0
10	HF2-RF3		6.1	0.042	5.5	2.3	17
11	HF2-RF4		7.1	0.08	4.8	2.3	21
12	HF2-RF5		7.2	0.08	9.4	3.9	50
13	HF3-F		9.2	0.015	0.2	–	0
14	HF3-RF1		8.8	0.027	3.3	0.3	0
15	HF3-RF2	AG	5.9	0.042	5.2	0.3	0
16	HF3-RF3		7.7	0.088	5.6	0.8	1
17	HF3-RF4		5.9	0.088	10.5	1.8	15
18	HF4-F		10.6	0.008	0.24	–	0
19	HF4-RF1	fgDG	9.0	0.01	1.8	–	1
20	HF4-RF2		8.8	0.012	2.1	–	0
21	HF4-RF3			Leakage behind fracture			0
22	HF5-F		9.0	–	–	–	0
23	HF5-RF1	fgDG	8.6	0.022	4.3	0.09	0
24	HF5-RF2		8.7	0.117	6.5	0.09	0
25	HF5-RF3		8.8	0.142	3.8	–	0
26	HF6-F		11.3	0.082	8.7	0.14	15
27	HF6-RF1	fgG	4.8	0.095	5.2	0.14	5
28	HF6-RF2		2.9	0.107	5.1	0.14	5
29	HF6-RF3		3.0	0.115	5.2	0.10	3

of relocated events were manually reviewed. Noise events were identified based on their waveform signature as well as their time and location of occurrence and excluded from the final catalogue. The remaining catalogue consists of 196 relocated AE events (Appendix A). Many more AE events with poor signal-to-noise ratios that could not be localized in this first analysis and need further investigation were recognized during manually reviewing the waveform. All AE events recognized occurred during the fracturing time periods. The relocated AE events are listed together with specific hydraulic test data for all six HF and refracturing phases in Table 3. In the following, we discuss the relocated AE event catalogue from Appendix A.

All relocated seismic AE events are shown in map view and side view in Fig. 8. AE events recorded during the different fracture experiments clearly delineate the fractures and display differences between the different hydraulic fractures generated. The pulse HF test in fine grained diorite gabbro (experiment HF5) did not generate seismic signals relocatable by the *in situ* monitoring array (Fig. 8).

The numbers of AE events differ between different fracture experiments (Table 3). A graphical representation is given in Fig. 8(c). For some fracture experiments only one (Fig. 8c, HF4 continuous) or no AE event (Fig. 8c, HF5 pulse injection) is localized. Manual review of waveforms of all triggers revealed that no seismic event was identified outside of the HF periods. Fracture experiments differ in injection flow rate, the geological setting, borehole length and the hydraulic test equipment.

Below, the focus is on the outline of experiment HF2 (conventional, continuous water injection) and experiment HF3 (progressive water injection) generated in the AG formation. In Fig. 9, corresponding AE events, pressure and flow rate are plotted versus time. While AE events are observed during all refracturing phases (except RF2) of conventional HF2 (Fig. 9a), in experiment HF3 using progressive water injection with alternating pressurization and depressurization phases, AE events occur in the third and fourth refracturing stage only (Fig. 9b).

Note that the continuous AE recording was not running during HF2-RF2. Thus, HF2-RF2 was terminated prematurely and the experiment HF2 continued with HF2-RF3. No AE occurs before the fracture breakdown pressure P_c in the progressive water injection experiment is reached despite the steady increase of flow rate for the last three bands.

Results can be summarized as follows. HF2 generated AE´s both during the generation (initial fracture phase = 7 events) and the propagation of the fracture (Fig. 8c, RF1 = 6 events, RF3 = 17 events, RF4 = 21 events, and RF5 = 50 events). The first AE event during the initial fracture phase was recorded when the injection pressure reached $P = 9.4$ MPa for the first time (Fig. 9a). Most AE events occurred during the fracture and refracture phases with injection pressures between 10.8 and 9.0 MPa. In addition, one AE event was observed during packer inflation before the initiation of HF2, when injection pressure was zero MPa (Fig. 9a). AE events recorded during the initial fracture phase are located at close

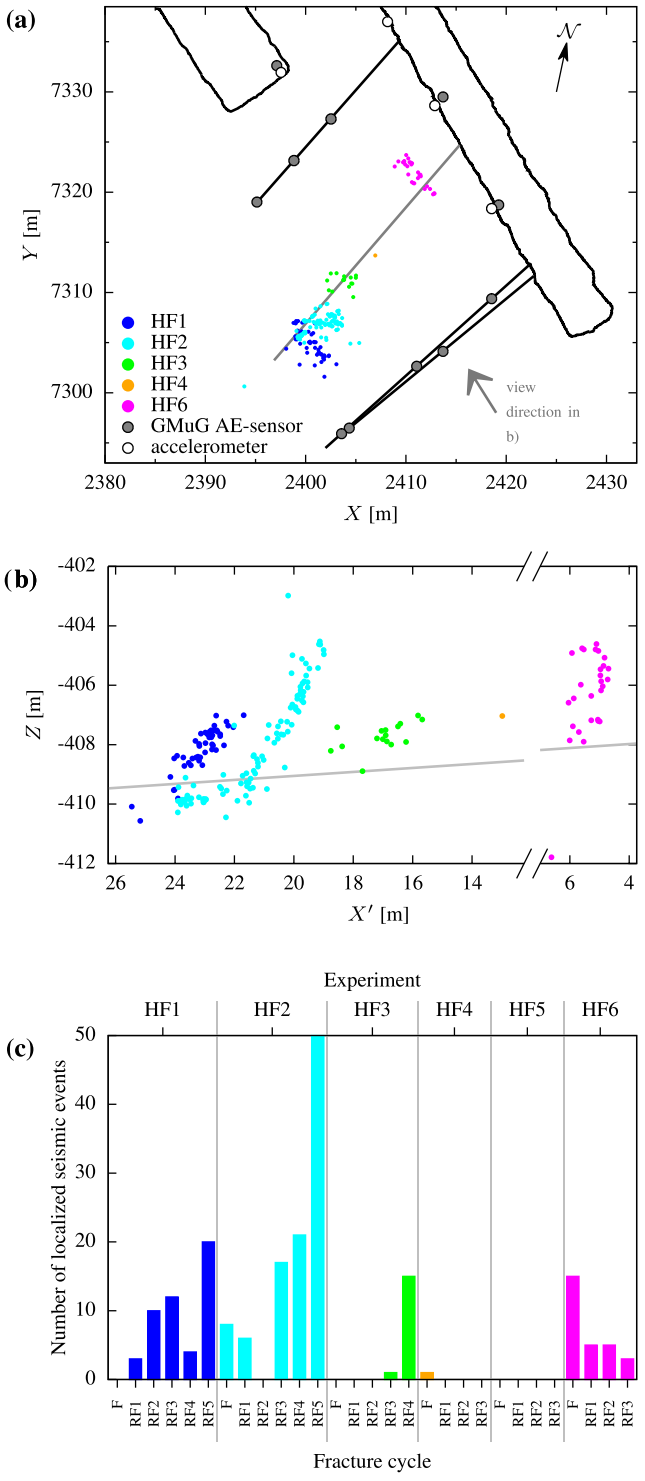

Figure 8. Seismic AE events presented in map view (a), side view (b) and (c) versus time in histogram. For side view the coordinate system was rotated [view angle shown by arrow in (a)] to indicate the preferred fracture traces. The seismic AE activity outlines the fractures of the different fracture experiments. Solid black lines outline the tunnel at the experimental site. Thin black lines outline the long monitoring boreholes. The solid grey line outlines fracturing borehole F1. Circles symbolize the sensors (grey, AE sensor; white, Accelerometer) of the AE monitoring network.

distance (0.1–1.3 m) to borehole F1 (Figs 8a and b). During refracs, AE events migrate both upwards and along the borehole towards the fracture area of HF1.

For example, after RF2 AE events cover the depth interval between 408 and 410 m whereas the depth interval between 404 and 411 m is seismically active during RF5 (Figs 8a and b, and 9a). AE events migrating upwards outline a plane (strike 133°, dip 62°) that is extending up to 6.7 m away from borehole F1 (Fig. 8).

In experiment HF3 (progressive water injection), no seismicity was recorded during the initial fracturing ($P \leq 9.2$ MPa), nor RF1 and RF2 ($P \leq 10.4$ MPa), see Fig. 9(b). During RF3 one AE event was recorded ($P = 11.3$). During RF4 at $P = 10.2$ to 11.0 MPa, 15 AE events were located. All events occurred during the fracture phase and no event during shut-in. The first event recorded during HF3-RF3 occurred at 1.47 m distance from borehole F1 (Figs 8a and b). Events recorded during RF4 occurred at distances between 0.85 and 2.30 m. In contrast to the observations in experiment HF2, no clear migration is visible for AE events recorded during experiment HF3 (progressive water injection). All but one event are located in the depth interval 407–408.2 m (Fig. 8, green dots). The events do not display a clear structure but cluster in a cloud without outlining a clear fracture plane, indicating that fluids did not possibly flow into a single hydraulic fracture.

For all fractures, the preliminary results suggest that the maximum AE magnitude is increasing with time (Fig. 9).

In Table 4, the results of the *in situ* AE monitoring are compared to the results from the impression packer test, which documents fractures visible after HF inside borehole F1. For HF2 it was found that the impression packer results coincide within 16 cm with the location, within 5° of the azimuth, and within 2° of the dip outlined by AE activity. It follows that both methods confirm the formation of a new macrofracture oriented approximately in east–west orientation with 60° dip towards south (Fig. 10). Moreover by using localized AE events it is now possible to estimate the upward extension of the macrofracture to 6.7 m.

For comparison we show the stress tensors closest to our study site from Ask (2006, fig. 9C, tensor at depth level 330 m from HF, 380 m from overcoring) in Fig. 10. The maximum horizontal stress is perpendicular to our fracturing borehole ($S_1 = S_H$). The intermediate principal stress is the vertical stress ($S_2 = S_V$) aligned with the borehole orientation, and the least principal stress is the minimum horizontal stress ($S_3 = S_h$).

The comparison between the results of the impression packer test and the *in situ* AE monitoring of experiment HF3 (progressive water injection) are less obvious. Two planes are identified by the impression packer at borehole lengths of 19.24 and 18.72 m (Table 4). One plane is oriented perpendicular to borehole F1 (Fig. 10, dip 84°), the other plane is tilted by 25° with respect to F1 alignment (Fig. 10, dip 47°). The AE events located nearest to borehole F1 is located at a borehole length of 17.44 m (in 0.85 m distance to F1), see Figs 8(a) and (b). Moreover, as discussed above, no clear planar structure can be extracted from the AE activity, as the events cluster in a cloud like structure (Figs 8a and b). For this reason, the formation of a single macrofracture can neither be confirmed nor be neglected at the moment. Further integrated analysis is necessary to conclude on the fractures generated by progressive water injection treatment with frequent bands of pressurization and depressurization. Aseismic deformation, the opening of pre-existing fractures or the formation of a fracture net rather than a macrofracture cannot be excluded based on the initial analysis.

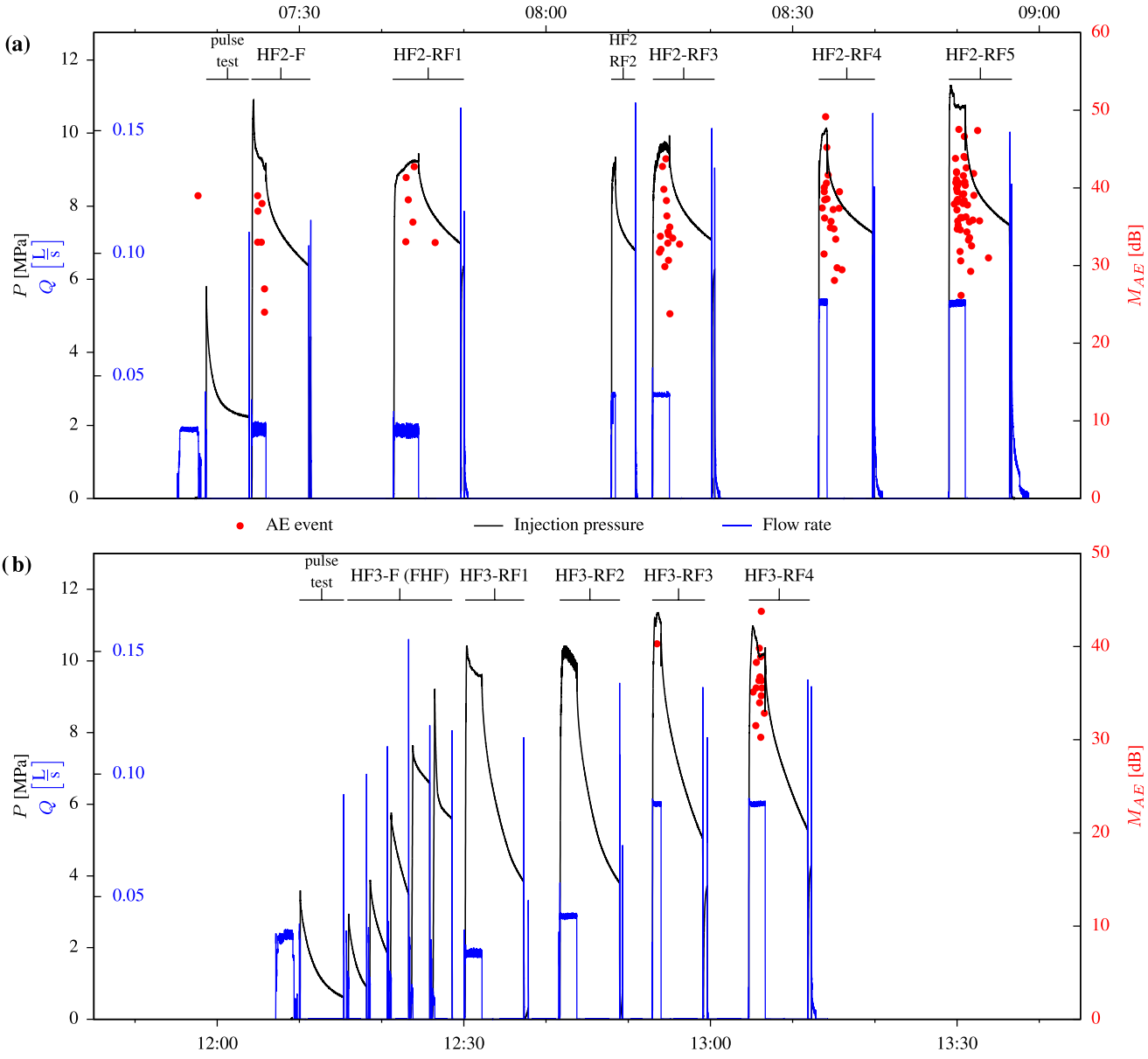

Figure 9. Injection pressure (P), flow rate Q (left axis) and AE magnitude (M_{AE}, right axis) for hydraulic fractures generated with two different fluid injection schemes: (a) conventional, continuous water injection experiment (HF2) and (b) progressive water injection experiment (HF3). For each refrac cycle the first AE event is observed at increasing pressure levels: $P = 9.08$ MPa, $P = 9.63$ MPa, $P = 9.93$ MPa and $P = 10.82$ MPa for the first AE event at RF1, RF3, RF4 and RF5, respectively. Some AE events occurred in the early shut-in phase (initial fracture phase = 0 events, RF1 = 1 event, RF3 = 4 events, RF4 = 11 events and RF5 = 16 events) with injection pressure $P \geq 7.7$ MPa.

Table 4. Comparison of fracture orientation from impression packer and AE activity results for three hydraulic fractures generated in Ävrö granodiorite (HF1–HF3). Note: Image packer was inserted after first refrac for HF1 and after the last refrac for HF2 and HF3. Borehole length of AE according to AE event located closest to F1. The fracture orientations are shown in Fig. 10.

	HF1 - single fracture		**HF2 - single fracture**		**HF3 - double fracture**	
	Impression packer	AE hypocentres	Impression packer	AE hypocentres	Impression packer	AE hypocentres
Azimuth (°N)	158	138	123	118	56 / 121	No plane
Dip (°)	74	45	60	62	47 / 84	No plane
BH length (m)	24.84	24.56	22.49	22.65	18.72 / 19.24	17.44
Extension (m)	Unknown	5.3	Unknown	6.7	Unknown	2.3

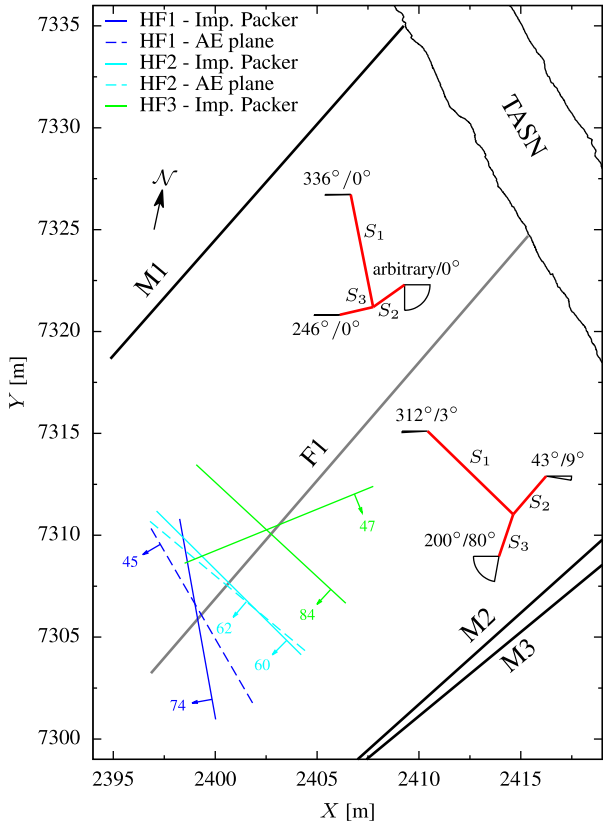

Figure 10. Fracture locations for HF1–HF3 from Table 4 in comparison to stress data. The orientation of the lines corresponds to the azimuth of the fractures, the dip direction is indicated by the adjacent arrow with the dip angle given in degree. The size of the lines is not related to the fracture extent. Fracture location estimates by impression packer are shown as solid lines, while fracture plane estimates from the AE distribution are shown as dashed lines. The AE based estimates are for HF1 and HF2 only, for HF3 the number of localized AE's is insufficient. The impression packer showed two fracture openings for HF3. Colour coding is analogue to Fig. 8. Two stress tensors from Ask (2006) closest to our study site are shown: Upper tensor is for the 330 m depth level from HF solutions ($S_1 = 20.9$ MPa, $S_2 = 8.7$ MPa, $S_3 = 6.7$ MPa), lower tensor is for the 380 m depth level from overcoring solutions ($S_1 = 22.6$ MPa, $S_2 = 9.5$ MPa, $S_3 = 8.1$ MPa). Stresses are viewed from above and projected onto the horizontal plane. The length of each vector is proportional to the corresponding stress magnitude. The fans at the vector tips describe the dip of the stress vector.

4.3 Microseismicity monitoring results

All stages of the experiment (Table 2) were monitored by the short period MS networks as well as the broad-band seismic stations. First analysis indicates that HF induced events did not radiate sufficient energy to be recorded above the noise level between 4 and 400 Hz, or were completely absent. With MS stations we have not detected clear, network-wide high frequency signals during the time of the fracturing and refracturing tests. However, single tracks of the 4.5 and 28 Hz borehole geophones need to be investigated in detail, in particular in the near field of the borehole F1 (see Fig. 4a, borehole geophones). This is because the signals may have been strongly attenuated from intrinsic damping or scattering effects. The absence of recorded MS events is unexpected since the AE network detected signals during the HF experiments in the frequency range from 1 to 100 kHz (Fig. 7). This frequency band, however, does not match the frequency band of the installed short-period MS sensors. Three borehole geophones in TASN (Fig. 4b, channels 14, 22, 23) indicate an MS event, most probably associated with RF3. No correlation was found with other seismic channels.

Despite the absence of clear HF induced signals between 4 and 400 Hz, we could identify HF associated signals at very low frequencies of some minutes duration. Fig. 11 shows the horizontal components of a broad-band sensor, which was installed in tunnel TASN close to borehole F1 (see Fig. 4b, grey dot in tunnel TASN) during experiment HF2 and HF3. A linear trend has been removed from the original data and the data were low pass filtered in the Z, N, and E components. The excursion on the horizontal components have durations in the range of a few hundred seconds, longer than the eigenperiod of the sensors, and are interpreted as tilt induced response of the seismometer. The HF2 experiment started with an initial packer test at 7:20AM, followed by the frac and five refracs. For injection pressure larger than 9 MPa the signals from the horizontal components indicate a low frequency tilt which is increasing in amplitude with each refrac cycle. The sequence of signals during HF3 shows a similar pattern (Fig. 11b). Note that during the experiment HF3 an M_W 5.1 earthquake occurred along the Reykjanes Ridge which is registered in the broad-band recording (Fig. 11b, EQ).

Tilt induced signals from broad-band sensor could be detected in several HF experiments. The tilt excursions can be explained if an intact part of the rock is fractured to a significant length during the initial fracturing cycles and for an injection pressure of about 9 MPa. Then the fracture is being gradually enlarged with subsequent refracturing cycles due to the increasing amount of pumped water (Fig. 5). The observed increase in seismic amplitude with each new refrac cycle possibly correlates with an increase in AE event magnitudes (Fig. 9a) and an increase in volume of the mobilized fracture with increasing fluid volume. After the last re-fracturing stage and during the bleed-off phase, the flipped polarity of the tilt excursion result (e.g. Fig. 11a) indicates the partial closure of the open hydraulic fracture.

4.4 Electromagnetic monitoring results

In the following results from EME measurements are presented in the frequency range between 35 and 50 kHz. With the AE in the same frequency range, it seems to be the most appropriate to follow fracture processes. EME, using Cerescope, are represented by the number of emissions N_E per time (parameter A). The measurements of these parameters account for the geogenic discrimination level representing the EM background (discrimination level: 27; gain: 7) by calibrating the instrument in the electrically quiet tunnel TASU (Fig. 4b).

Together with hydraulic data (flow rate and interval pressure) of HF2, parameter A is shown in Fig. 12 for the sensor that is oriented perpendicular the fracture plane. From the variation of parameter A with flow rate, it is obvious that the geogenic background level is mainly perturbed by the operation of the pump used for injection. Under pumping condition, this parameter increases from its base level by about 3–4 $N_E\,ms^{-1}$ up to 7.5 $N_E\,ms^{-1}$. Fluid circulation in the rock is unlikely to be the cause of this level change, since variation of parameter A is not observed at high flow rates during backflow at the end of each fracturing or refracturing stage. Apart from the first preparatory operation at about 2 $L\,s^{-1}$ and zero pressure (between 7:15 and 7:18), after which N_E falls back to its original value, the background level at pressure shut-in is observed to be about 0.5 $N_E\,ms^{-1}$ lower compared to the value before the injection step. With decreasing pressure during the ongoing shut-in

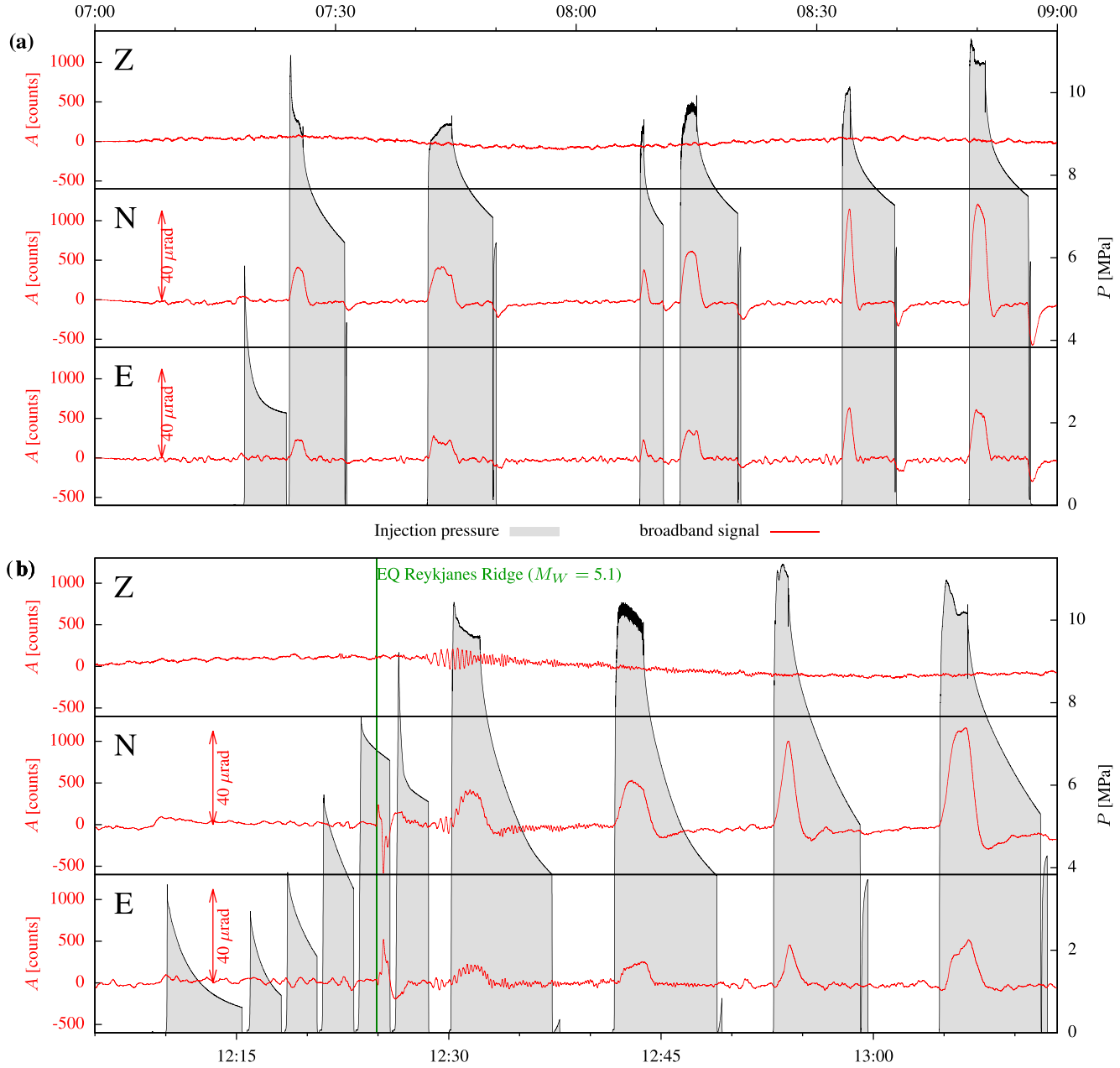

Figure 11. Recordings of broad-band sensor in tunnel TASN. The linear trend has been removed from the data (Z-, N- and E-components in counts) and a low-pass filter was applied (10^{-5}–10^{-1} Hz). (a) Packer test at 5 m depth, and HF2 experiment at 25 m borehole depth in borehole F1. While the initial fracturing stage of HF2 has produced no obvious anomalous signal in the horizontal components, by contrast, a tilt is observed in both horizontal components (N, E) during subsequent refracturing stages. (b) HF3 experiment at 22.5 m borehole depth. During the test HF3 on 4th June, the signals in the N- and E-component of the seismometer detected a tilt in the initial fracture stage. The following refracturing stages show an increase in tilt amplitude. The onset of an earthquake occurring at the Reykjanes Ridge is indicated by the green line.

phase of the first breakdown and the following RF1 to RF5, N_E increases with time. This increase continuous beyond the shut-in phase during flow-back measurements and preparation time for the follow-up RF step. It results in a total increase of about 1.5 N_E ms^{-1} during the period, when the pump is off. This increase neither correlates with the electric noise level of the pump, nor is it an artefact caused be the different sensors. The latter can be demonstrated by the fact that this behaviour has been observed in different experiments, although the sensors have been exchanged during tests.

5 DISCUSSION

In AG, the comparison of fracture breakdown pressure (P_c) from single flow rate conventional, continuous water injection experiments (HF) and multiple-flow rate injection tests (progressive, dynamic pulse injection) simulating FHF revealed a reduction of the breakdown pressure by 30 per cent (comparison of experiment HF1 with HF3) and 15 per cent (comparison of experiment HF2 with HF3), respectively. During the five bands of progressively increasing

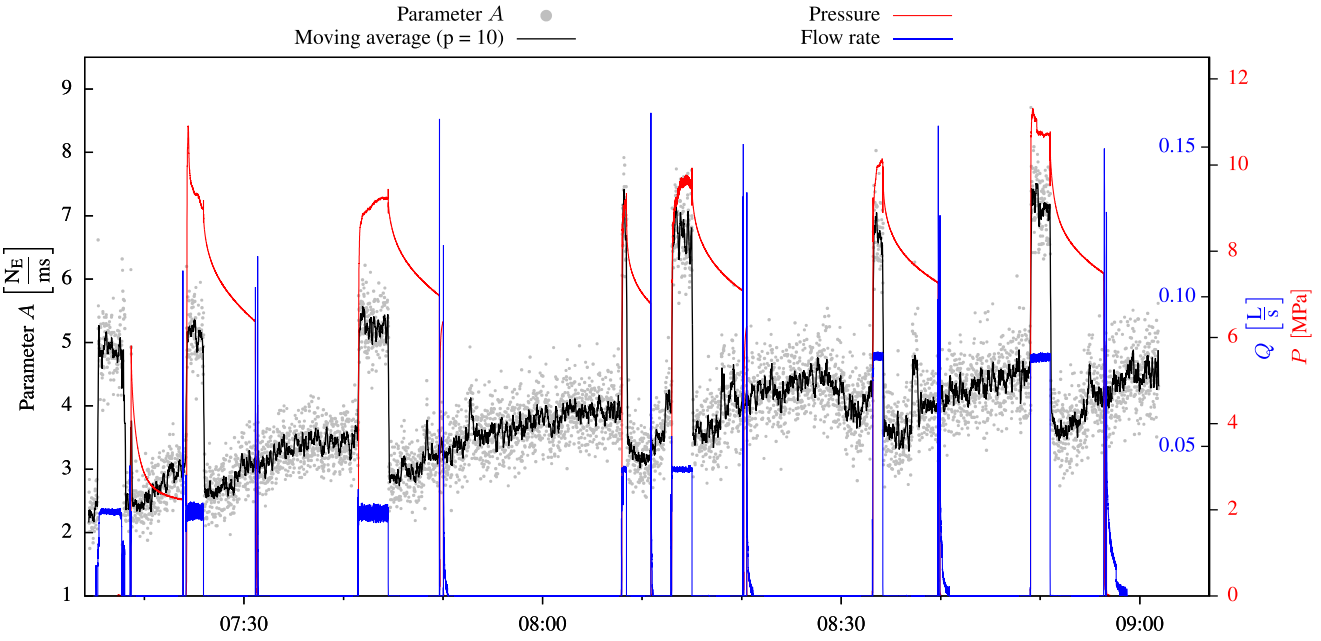

Figure 12. Number of electromagnetic emission N_E in the frequency range of 35–50 kHz acquired subperpendicular with an azimuth 40° to the fracture plane generated during the conventional hydraulic fracturing test HF2 compared to injection flow rate and pressure.

target pressure interrupted by four depressurization phases in between (experiment HF3), no seismicity was recorded with the *in situ* AE trigger system. In fgDG, the pulse hydraulic test (HF5) showed a pressure drop at the third cycle of the treatment interpreted as indication of rock failure with a corresponding pressure approximately 15 per cent lower compared to the fracture breakdown pressure of the conventional treatment HF4 in the same formation. During the pulse injection test, again no seismicity could be detected with the *in situ* AE trigger system. In the fine grained granite (fgG) close to the tunnel wall, seismicity was observed during conventional, continuous water injection (experiment HF6). No fatigue treatment could be performed in this more brittle material because no more testing interval was remaining.

It has to be pointed out that the lowering of fracture breakdown pressure and lowering of associated seismicity due to different injection styles used are tentative results. They are based on a limited amount of tests (six) in naturally fractured crystalline rock (three rock types) for logistic and budgetary reasons. Future analysis of data will focus on better understanding and comparison of activated source mechanisms and seismic events for different fluid injection schemes. Nevertheless, the findings from our underground experiments are in line with laboratory testing results supported by much more test specimens. In general, the results from our *in situ* tests will help to shed light on the scaling problem of the hydraulic fracture growth process in hard rock.

From laboratory tests on rock cores (diameter approximately 10 cm and length 20 cm), and tests on large concrete blocks (one cubic metre in size), Jiráková *et al.* (2015) found a lower fracture breakdown pressure by 18 per cent when cyclic injection was applied instead of using continuous increase of water injection into the specimens. The same tendency (lowering the fracture breakdown pressure) was found in testing laboratory granite core samples with 5 cm diameter and 10 cm length by cyclic water fracturing (Zhuang *et al.* 2016).

In addition, Zhuang *et al.* (2016) investigated the fracture pattern from conventional and cyclic water injection by X-Ray CT measurements. Similar to our findings from the *in situ* testing (HF1 and HF2 single fracture, HF3 double fracture) there seems to be a more complex fracture pattern resulting from cyclic compared to continuous water injection. The reason for this may be a different energy release process operating at the fracture tip in fatigue testing compared to conventional HF.

Our first field results from the *in situ* trigger system demonstrate clearly that *in situ* HF in hard rock in four of six cases is accompanied by AE events, which outline the fracture planes and display different behaviours, potentially correlated to differences in the HF procedure. AE activity was not recorded for HF4 (conventional) and HF5 (pulse injection) that were both generated in fine grained diorite gabbro. This may be explained either by AE below the detection threshold, by aseismic nucleation and growth of HF in different rock material, or by using fracturing equipment of different companies. It should be pointed out that variations in background noise level during the different fracture methods are likely to occur and further analysis to reduce the noise levels must be considered.

The distribution of AE in the different experiments leads to total radii of the fractures generated during HF1, HF2 and HF3 of about 1 to 3.5 m (Table 4, fracture extension). Based on the observable frequency content of the recorded events in this study and the findings of Kwiatek *et al.* (2011) for AE events related to excavations in a hard rock mine in South Africa, it is assumed that the recorded AE´s correspond to the fractures with source dimensions of <1 dm and moment magnitudes $M_W < -4.5$.

The AE data catalogue built from the recordings in triggering mode (Table A1 in Appendix A) is not complete and has varying magnitudes of completeness. Manual review of data already showed that additional seismic events are present, but could not be localized using the *in situ* localization algorithm. These so far unlocated AE events show poor signal-to-noise ratios and correspond presumably to small seismic events. In addition, events can be missed in

trigger mode recording, when the measuring system is busy processing a preceding event or when several events occur within the 32 ms recording window. On average, four AE events can be processed per second. In order to derive a complete catalogue, data of all sensors of the AE network were recorded in continuous mode during the experiments. Offline processing of the data stream will allow analysing the data without loss and applying advance trigger algorithms. It is therefore expected that the resolution of AE monitoring will increase in future analysis. The distribution of AE hypocentres in space and time suggests that all fractures detected seem to grow upwards. Note that AE clusters HF1, HF2, HF3, and HF6 elongate in side view indicating upward migration along differently inclined pre-existing discontinuities (Fig. 8b). This may indicate that fluid injection caused opening and activation of previously undetected fractures at least at some distance to the borehole wall. Only few events below the level of borehole F1 are observed (Fig. 8). This result is likely to be influenced by the network geometry since all sensors are located above F1 due to requirements in sensor installation. Accordingly, the network sensitivity below borehole F1 is significantly less than above F1. It is possible that AE events originated from significantly below F1 are missed. On the other hand, stress gradients or effective buoyancy effects can also explain unidirectional fracture growth (Dahm 2000; Dahm *et al.* 2010).

The correlation between AE events, injection pressure, and flow rate are well documented in this document (Fig. 9). Similar correlations were shown for HF stimulation of a geothermal reservoir (Plenkers *et al.* 2012).

Despite of the usual uncertainties in the automatic picking algorithm as well as in the velocity model, the uncertainty of the automatic localization of most AE events is in the order of a few decimetre only, owing to the three-dimensional outlay of the AE monitoring network. We conclude that the general orientation and extension of fractures observed from AE hypocentres are reliable. Detailed features might be affected by location uncertainty and require more elaborative processing techniques to improve the precision of locations (e.g. cross-correlation double-difference technique, work in progress). It was shown by Naoi *et al.* (2015) that by applying the double-difference technique to AE events recorded *in situ* it becomes possible to image even small details of the fracture such as bending, kinks or branching. The quality of the waveforms recorded with the *in situ* AE monitoring network is excellent. Many AE events are recorded with good signal-to-noise ratios. It follows that the application of advanced seismological analysis techniques such as moment tensor analysis and source parameter assessment are possible and will provide additional insights on the fracture process. Combining triggered recording during the *in situ* AE monitoring with simultaneously recording the AE waveforms continuously was beneficial for the project, because it allowed to gain information in (near) real time on AE event location and therefore on fracture expansion while to the same time storing all waveform data without any losses.

The location and orientation of fractures outlined by the AE hypocentres correlate well with the location of the injection in borehole F1 and result of the impression packer. Using impression packers in combination with AE *in situ* monitoring it is possible to monitor not only the fracture orientation at the fracture borehole, but also in the rock volume away from the fracture borehole. This allows monitoring deviations in fracture orientation, the temporal evolution of fractures growth as well as the fracture extension.

Another interesting observation is the aseismic response of the rock mass during the first injection leading to the breakdown and fracture initiation at the borehole wall. The seismic response and fracture propagation develop during the successive refracturing. Guglielmi *et al.* (2015) are reporting that initial fluid injection into a fault intersection of a borehole in limestone was aseismic and became seismic when the radius of pressurization front and slip zone reached approximately 8 m. The total volume injected in this small fault reactivation experiment was 950 L over about half an hour, at 282 m depth in cretaceous limestone in the underground laboratory LSBB in southeastern France. In our experiment, the total amount of only 23 L (HF3) to 29 L (HF1) was injected into a crystalline rock mass at 410 m depth. From the analysis of back flow, an amount of 13 L was recovered during HF1 and 3 L during HF3. This can indicate a more complex fracture pattern evolving during the fatigue treatment compared to conventional HF operation. The detailed analysis of the permeability enhancement process, however, will be presented in an accompanying paper.

Overall, further investigations are necessary to understand the parameters influencing the AE activity and magnitudes. Potential parameters are not only the initial rock condition and the influence of pre-existing fractures, but also the parameters of the HF like pressure and flow rate applied. Future in depth and integrated analysis of the unique combination of different data sets will increase the resolution and clarify the energy partition in the test performed in hard crystalline rock with advanced fluid injection schemes.

The observed tilt signals in the horizontal components of the broad-band sensor reflect a tilt around a horizontal axis (40 μrad), see Fig. 11. However, a simple geometrical relation could not be derived and we assume that the tilt axis is influenced by the free surface of the gallery and possibly by pre-existing fractures in the rock mass. Strain tilt coupling from a cavity effect is well known from tiltmeters installed in underground observatories (Harrison 1976; Emter & Zürn 1985; Gebauer *et al.* 2010; Forbriger 2012). Also, Jeffrey *et al.* (2009) used tiltmeters in HF experiments. The tilt induced signals from broad-band recordings related to HF experiments in crystalline rock in the near field in this study, however, are unique observations (Fig. 11), and to our knowledge have not been reported before. The data may provide additional and independent information on the fracture size, growth and fracture orientation in the process of fracture modelling, apart from the analysis of AE event hypocentres.

The observation of increasing number of EM emission in the frequency range between 37 and 50 kHz with decreasing pressure in the shut-in phase is an interesting outcome of EM monitoring. It suggests a possible trend in EM signal in the time period that is assumed to represent the closure of the fracture walls before the subsequent RF tests, when determining the hydraulic tensile strength of the rock formation. A correlation between electric current and stress has been observed earlier in the laboratory experiment (Freund *et al.* 2006), where the differential stress represented about one third of the failure strength of the granite. Further analysis is necessary to confirm the origin of the relation between EME and hydraulic data.

Choosing the best monitoring equipment for *in situ* fracture experiments *a priori* comes with many unknowns. We find that our multisensor monitoring approach was successful. Different sensors were able to monitor different aspects of the experiment. No sensor was able to record all the different rock responses. Moreover it is important to note that some signals are easily missed if restricting the monitoring to one kind of sensors only. For example we find that the Wilcoxon accelerometers were not able to record AE events detected with the *in situ* AE sensors, despite of the fact that AE events were present in the frequency range of the accelerometer. This observation stresses once more that *in situ* AE sensors are

beneficial over pendulum based seismometers in the kHz range, because they are much more sensitive. On the other hand we also find that broad-band sensors were able to observe a tilt signal at low frequencies during fracture times without AE activity, thus giving insights on fractures that could not be recovered using AE sensors. Our results therefore demonstrate clearly that the monitoring of *in situ* fracture experiments requires the monitoring of a broad frequency range of approximately 10 mHz to 100 kHz.

In conclusion, amplitude and rate of deep fluid injection experiments (HF, or fault reactivation), together with the size of volume affected, dictate the characteristics of the monitoring system to be used. According to Cornet (2016), rupture slip rates range from 1000 m s^{-1} (seismic slip motions) to 1 m h^{-1} (aseismic slip motion) and probably lower. Similarly, slip displacements range from μm to cm. Their proper monitoring requires complementary sensors and techniques so as to cover the complete range of amplitudes and rates of stress perturbations in the experiment.

6 CONCLUSIONS

Based on the analysis of six hydraulic fractures propagated in a horizontal borehole with three different water injection schemes (continuous, progressive and pulse injection), and mapped by an extensive monitoring array (AE, MS and EM) in a Swedish hard rock laboratory at 410 m depth, we draw the following conclusions.

(i) In the framework of the limited number of *in situ* tests performed, a tendency of lower fracture breakdown pressure was found when single-flow rate, conventional fluid injection was replaced by multiple-flow rate, progressive or dynamic pulse injection. Also, the total number of seismic events and their magnitude is found to be influenced by the injection style. In AG, AE events started at a later stage and the total number of events was smaller when the continuous injection scheme was replaced by multiple flow rate injections with progressively increasing target pressure and several phases of depressurization.

(ii) For all fractures, our first results suggest that the maximum magnitude of AE signals increases with time in the fracturing experiment, that is, the maximum magnitude of each refracture cycle increases with the number of cycles.

(iii) The *in situ* AE monitoring network successfully recorded seismic events in the frequency range above 1 kHz for most, but not all hydraulic fractures. AEs clearly outline not only the fractures location, its orientation, and expansion, but also the fractures temporal evolution. Clear differences between different hydraulic fractures are visible which need further investigation. With these new insights into the common HF operations and hydraulic stress measurement together with *in situ* AE monitoring is seen valuable.

(iv) Small rock deformation (40 μrad) induced by HF in a horizontal borehole was monitored with a broad-band seismometer operating in a tunnel in the near field. This finding allows obtaining additional information about the stability of the rock mass, and the response of the rock mass to loading. This can be used as a secondary source of information for tracking and modelling the fracture growth process at different stages.

(v) The EM monitoring in an electrically fully equipped underground research laboratory showed clear variations in the number of EME in the injection and shut-in intervals and with respect to the background level.

(vi) To understand the physics of hydraulic fracture nucleation, propagation and arrest, *in situ* experiments at mine-scale can help only if the monitoring system is adapted to the frequency range expected, approximately from 10 mHz to 100 kHz. Apart from the seismic energy radiated by the fracture, also aseismic slip and heat dissipation are worth to be detected while the pumped in hydraulic energy is documented by advanced fluid injection protocols.

ACKNOWLEDGEMENTS

The Äspö HRL is owned by the Swedish Nuclear Fuel and Waste Management CO (SKB) and has been in operation since 1995. In close cooperation with the municipality of Oskarshamn, SKB has supported the formation of Nova FoU (R & D) with the aim to use the Äspö facilities for research and development in other sectors and branches. The geothermal project Nova 54-14-1 described in this manuscript is one of those.

Nova project 54-14-1 was financially supported by GFZ German Research Center for Geosciences (75 per cent), KIT Karlsruhe Institute of Technology (15 per cent) and Nova Center for University Studies, Research and Development (10 per cent). An additional in-kind contribution of SKB for using Äspö Hard Rock Laboratory as test site for geothermal research is greatly acknowledged.

All boreholes were drilled with required high precision for AE monitoring in time with help of Göran Nilsson Consult, and the companies Drillcon Core AB Nora and MiRo Diamanthåltagning AB Kalmar. Hydraulic testing was performed by MeSy Solexperts Bochum (Germany) and Industrial Saftey Assessment Technicians ISATech Prague (Czech Republic). We like to thank Gerd Klee (MeSy Solexperets) and Hana Semikova (ISATech) for good collaboration underground.

Monitoring equipment has been provided by geophysical instrumentation pool GIPP of GFZ Potsdam, and KIT Karlsruhe, Germany. We thank the GFZ engineers Stefan Mikulla and Peter Neuendorf for their help in preparing and testing the microseismic instrumentation. Stefan Mikulla also helped in installing microseismic equipment underground at Äspö HRL. Monitoring equipment for the AE monitoring network was provided and operated by GMuG mbH, Bad Nauheim Germany. We thank Thomas Fischer for his efforts to help with the smooth operation underground.

Anonymous reviewers with demonstrated expertise in HF commented and corrected an earlier version of this manuscript. We like to thank the reviewers for improving the quality of this paper.

REFERENCES

Allen, R., 1982. Automatic phase pickers: their present use and future prospects, *Bull. seism. Soc. Am.,* **72**(6), S225–S242.

Allen, R.V., 1978. Automatic earthquake recognition and timing from single traces, *Bull. seism. Soc. Am.,* **68**(5), 1521–1532.

Ask, D., 2003. Evaluation of measurement-related uncertainties in the analysis of overcoring rock stress data from Äspö HRL, Sweden: a case study, *Int. J. Rock Mech. Min. Sci.,* **40**(7–8), 1173–1187.

Ask, D., 2006. Measurement-related uncertainties in overcoring data at the Äspö HRL, Sweden. Part 2: Biaxial tests of CSIRO HI overcore samples, *Int. J. Rock Mech. Min. Sci.,* **43**(1), 127–138.

Bohnhoff, M., Dresen, G., Ellsworth, W.L. & Ito, H., 2009. Passive seismic monitoring of natural and induced earthquakes: Case studies, future directions and socio-economic relevance, in *New Frontiers in Integrated Solid Earth Sciences,* pp. 261–285, eds Cloetingh, S.A.P.L. & Negendank, J., Springer.

Cornet, F.H., 2016. Seismic and aseismic motions generated by fluid injections, *Geomech. Energy Environ.,* **5,** 42–54.

Dahi Taleghani, A. & Lorenzo, J., 2011. An alternative interpretation of microseismic events during hydraulic fracturing, in *Proc. SPE Hydraul. Fract. Technol. Conf.,* SPE–140468–MS, Society of Petroleum Engineers.

Dahm, T., 2000. Numerical simulations of the propagation path and the arrest of fluid-filled fractures in the Earth, *Geophys. J. Int.,* **141**(3), 623–638.

Dahm, T., 2001. Rupture dimensions and rupture processes of fluid-induced microcracks in salt rock, *J. Volcanol. Geotherm. Res.,* **109**(1–3), 149–162.

Dahm, T. & Krüger, F., 1999. Higher-degree moment tensor inversion using far-field broad-band recordings: theory and evaluation of the method with application to the 1994 Bolivia deep earthquake, *Geophys. J. Int.,* **137**(1), 35–50.

Dahm, T., Hainzl, S. & Fischer, T., 2010. Bidirectional and unidirectional fracture growth during hydrofracturing: role of driving stress gradients, *J. geophys. Res.,* **115**(12), 1–18.

Darnet, M., Maineult, A. & Marquis, G., 2004. On the origins of self-potential (SP) anomalies induced by water injections into geothermal reservoirs, *Geophys. Res. Lett.,* **31**(19), 1–5.

Döse, C., Strahle, A., Rauseus, G., Samuelsson, E. & Olsson, O., 2008. Revision of bips-orientations for geological objects in boreholes from forsmark and laxemar, *Tech. Rep.,* SKB-Report P-08-37, Swedish Nuclear Fuel and Waste Management Co.

Economides, M.J., Nolte, K.G., Ahmed, U. & Schlumberger, D., 2000. *Reservoir Stimulation,* vol. 18, Wiley.

Eisenblätter, J., 1988. Localisation of fracture planes during hydraulic fracturing experiments in a salt mine, in, *Acoustic Emission,* pp. 291–303, Deutsche Gesellschaft für Metallkunde e.V., Oberursel.

Eisenblätter, J. & Spies, T., 2000. Ein Magnitudenmaß für Schallemissionsanalyse und Mikroakustik, in *12. Kolloquium Schallemission, Berichtsband 72 der DGZfP,* pp. 29–41, Jena.

Ellsworth, W.L., 2013. Injection-Induced Earthquakes, *Science,* **341**(6142), 1 225 942–1 225 942.

Emsley, S., Olsson, O., Stenberg, L., Alheid, H. & Falls, S., 1997. Zedex - a study of damage and disturbance from tunnel excavation by blasting and tunnel boring, *Tech. Rep.,* SKB TR-97-30.

Emter, D. & Zürn, W., 1985. Observations of local elastic effects on earth tide tilts and strains, in *Earth Tides, Benchmark Pap. Geol. Ser.,* pp. 309–327, ed Harrison, J.C. & Van Nostrand, Reinhold.

Eydam, D. & Muñoz, G., 2011. The permanent magnetotelluric remote reference station, *Protok. über das 24. Schmucker-Weidelt-Kolloquium für Eleketromagnetische Tiefenforsch.,* **24,** 45–56.

Fenoglio, M.A., 1995. Magnetic and electric fields associated with changes in high pore pressure in fault zones: application to the Loma Prieta ULF emissions, *J. geophys. Res.,* **100**(B7), 12 951–12 958.

Fischer, T., Hainzl, S. & Dahm, T., 2009. The creation of an asymmetric hydraulic fracture as a result of driving stress gradients, *Geophys. J. Int.,* **179**(1), 634–639.

Forbriger, T., 2012. Recommendations for seismometer deployment and shielding, in *New Manual of Seismological Observatory Practice 2,* pp. 1–10, ed. Bormann, P., Deutsches GeoForschungsZentrum.

Freund, F.T., Takeuchi, A. & Lau, B.W.S., 2006. Electric currents streaming out of stressed igneous rocks–a step towards understanding pre-earthquake low frequency EM emissions, *Phys. Chem. Earth,* **31**(4–9), 389–396.

Gebauer, A., Steffen, H., Kroner, C. & Jahr, T., 2010. Finite element modelling of atmosphere loading effects on strain, tilt and displacement at multi-sensor stations, *Geophys. J. Int.,* **181**(3), 1593–1612.

Goertz, A., Riahi, N., Kraft, T. & Lambert, M., 2012. Modeling detection thresholds of microseismic monitoring networks, in *SEG Tech. Progr. Expand. Abstr. 2012,* pp. 1–6, Society of Exploration Geophysicists.

Guglielmi, Y., Cappa, F., Avouac, J.-P., Henry, P. & Elsworth, D., 2015. Seismicity triggered by fluid injection - induced aseismic slip, *Science,* **348**(6240), 1224–1227.

Hagag, W. & Obermeyer, H., 2016. Detection of active faults using EMR-Technique and Cerescope at Landau area in central Upper Rhine Graben, SW Germany, *J. Appl. Geophys.,* **124,** 117–129.

Haimson, B. & Cornet, F., 2003. ISRM Suggested Methods for rock stress estimation-Part 3: hydraulic fracturing (HF) and/or hydraulic testing of pre-existing fractures (HTPF), *Int. J. Rock Mech. Min. Sci.,* **40**(7–8), 1011–1020.

Harrison, J.C., 1976. Cavity and topographic effects in tilt and strain measurement, *J. geophys. Res.,* **81**(2), 319–328.

Jeffrey, R. *et al.*, 2009. Measuring hydraulic fracture growth in naturally fractured rock, in *SPE Annu. Tech. Conf. Exhib.,* pp. 1–19, doi:10.2118/124919-MS.

Jiráková, H., Frydrych, V., Vintera, J., Krásný, O. & Vaněček, M., 2015. Results of the Rock Hydraulic Fracturing Research Project, *Tunel - Undergr. Constr. Mag. Czech Tunneling Assoc. Slovak Tunneling Assoc.,* **24**(4), 57–64.

Klee, G. & Rummel, F., 2002. IPR-02-02 Rock stress measurements at the Äspö HRL Hydraulic fracturing in boreholes, *Tech. rep.,* SKB.

Krauß, F., Giese, R., Alexandrakis, C. & Buske, S., 2014. Seismic travel-time and attenuation tomography to characterize the excavation damaged zone and the surrounding rock mass of a newly excavated ramp and chamber, *Int. J. Rock Mech. Min. Sci.,* **70,** 524–532.

Kwiatek, G., Plenkers, K. & Dresen, G., 2011. Source parameters of picoseismicity recorded at Mponeng deep gold mine, South Africa: Implications for scaling relations, *Bull. seism. Soc. Am.,* **101**(6), 2592–2608.

Manthei, G. & Eisenblätter, J., 2008. Acoustic emission in study of rock stability, in *Acoustic Emission Testing,* pp. 239–310, eds Grosse, C. & Ohtsu, M., Springer.

Manthei, G., Eisenblätter, J. & Kamlot, P., 2003. Stress measurements in salt mines using a special hydraulic fracturing borehole tool, in *Geotechnical Measurement and Modelling,* pp. 355–360, eds Natau, O., Fecker, E. & Pimentel, E., CRC Press.

Mizutani, H., Ishido, T., Yokokura, T. & Ohnishi, S., 1976. Electrokinetic phenomena associated with earthquakes, *Geophys. Res. Lett.,* **3**(7), 365–368.

Murakami, H., Mizutani, H. & Nabetani, S., 1984. Self-potential anomalies associated with an active fault, *J. Geomagn. Geoelectr.,* **36**(9), 351–376.

Murakami, H., Hashimoto, T., Oshiman, N., Yamaguchi, S., Honkura, Y. & Sumitomo, N., 2008. Electrokinetic phenomena associated with a water injection experiment at the Nojima fault on Awaji Island, Japan, *Isl. Arc,* **10**(3–4), 244–251.

Naoi, M. *et al.*, 2015. Steady activity of microfractures on geological faults loaded by mining stress, *Tectonophysics,* **649,** 100–114.

Niitsuma, H., Nagano, K. & Hisamatsu, K., 1993. Analysis of acoustic emission from hydraulically induced tensile fracture of rock, *J. Acoust. Emiss.,* **11**(4), S1–S18.

Oth, A. & Picozzi, M., 2012. Structural health monitoring using wireless technologies: An ambient vibration test on the adolphe bridge, Luxembourg City, *Adv. Civ. Eng.,* **2012,** doi:10.1155/2012/876174.

Patel, S., Sondergeld, C. & Rai, C., 2016. Laboratory studies of cyclic injection hydraulic fracturing, in *SEG International Exposition and 86th Meeting,* pp. 3364–3368, doi:10.1190/segam2016-13969713.1.

Peacock, J.R., Thiel, S., Reid, P. & Heinson, G., 2012. Magnetotelluric monitoring of a fluid injection: Example from an enhanced geothermal system, *Geophys. Res. Lett.,* **39**(18), L18403, doi:10.1029/2012GL053080.

Philipp, J., Plenkers, K., Gärtner, G. & Teichmann, L., 2015. On the potential of In-Situ Acoustic Emission (AE) technology for the monitoring of dynamic processes in salt mines, in *Mechanical Behaviour of Salt VIII,* pp. 89–98, ed. Roberts, L., CRC Press.

Picozzi, M., Milkereit, C., Parolai, S., Jaeckel, K.-H., Veit, I., Fischer, J. & Zschau, J., 2010a. GFZ Wireless Seismic Array (GFZ-WISE), a wireless mesh network of seismic sensors: new perspectives for seismic noise array investigations and site monitoring, *Sensors,* **10**(4), 3280–3304.

Picozzi, M. *et al.*, 2010b. Wireless technologies for the monitoring of strategic civil infrastructures: An ambient vibration test on the Fatih Sultan Mehmet Suspension Bridge in Istanbul, Turkey, *Bull. Earthq. Eng.,* **8**(3), 671–691.

Plenkers, K., Kwiatek, G., Nakatani, M. & Dresen, G., 2010. Observation of seismic events with frequencies f >25 kHz at Mponeng Deep Gold Mine, South Africa, *Seismol. Res. Lett.,* **81**(3), 467–479.

Plenkers, K., Ritter, J.R.R. & Schindler, M., 2012. Low signal-to-noise event detection based on waveform stacking and cross-correlation: Application to a stimulation experiment, *J. Seismol.,* **17**(1), 27–49.

Rubinstein, J.L. & Mahani, A.B., 2015. Myths and Facts on wastewater injection, hydraulic fracturing, enhanced oil recovery, and induced seismicity, *Seismol. Res. Lett.,* **86**(4), 1060–1067.

Semíková, H., Bílý, P. & Krásný, O., 2014. Pulse hydraulic fracturing of a rock massif - the STIROMAS project, in *5th Int. Colloquim Gemechanics Geophys. - GECO,* p. 19, Ostrava and Karolinka.

Singhal, B.B.S. & Gupta, R.P., 1999. *Applied Hydrogeology of Fractured Rocks,* Springer Science & Business Media.

Sleefe, G., Warpinski, N. & Engler, B., 1995. The Use of Broadband Microseisms for Hydraulic Fracture Mapping, *SPE Form. Eval.,* **10**(4), 233–240.

Smart, K.J., Ofoegbu, G.I., Morris, A.P., McGinnis, R.N. & Ferrill, D.A., 2014. Geomechanical modeling of hydraulic fracturing: why mechanical stratigraphy, stress state, and pre-existing structure matter, *Am. Assoc. Pet. Geol. Bull.,* **98**(11), 2237–2261.

Stenberg, L., 2015. Geological and hydrogeological description of the Äspö extension area, *Tech. rep.,* SKB.

Suckale, J., 2009. Induced seismicity in hydrocarbonfields, in *Advances in Geophysics,* vol. 51, pp. 55–106, Elsevier, doi:10.1016/S0065-2687(09)05107-3.

van der Baan, M., Eaton, D. & Dusseault, M., 2013. Microseismic monitoring developments in hydraulic fracture stimulation, in *Effective and Sustainable Hydraulic Fracturing,* pp. 439–466, eds Bunger, A.P., McLennan, J. & Jeffrey, R., doi:10.5772/56444.

Yoon, J.S., Zang, A. & Stephansson, O., 2014. Numerical investigation on optimized stimulation of intact and naturally fractured deep geothermal reservoirs using hydro-mechanical coupled discrete particles joints model, *Geothermics,* **52,** 165–184.

Zang, A. & Stephansson, O., 2010. *Stress Field of the Earth's Crust,* Springer Science & Business Media.

Zang, A., Yoon, J.S., Stephansson, O. & Heidbach, O., 2013. Fatigue hydraulic fracturing by cyclic reservoir treatment enhances permeability and reduces induced seismicity, *Geophys. J. Int.,* **195**(2), 1282–1287.

Zang, A., Oye, V., Jousset, P., Deichmann, N., Gritto, R., McGarr, A., Majer, E. & Bruhn, D., 2014. Analysis of induced seismicity in geothermal reservoirs - An overview, *Geothermics,* **52,** 6–21.

Zhuang, L., Kim, K., Jung, S., Diaz, M., Park, S., Zang, A., Stephansson, O. & Yoon, J., 2016. Laboratory study on cyclic hydraulic fracturing of Pocheon granite in Korea, in *50th US Rock Mechanics/Geomechanics Symposium,* Houston, Texas, USA (26–29 June), no. 16-163, American Rock Mechanics Association.

APPENDIX A: LIST OF AE HYPOCENTRES

Table A1. List of AE hypocentres in ÄSPÖ96 coordinates.

Date	Time	*X*	*Y*	*Z*	Fracture
2015-06-03	10:04:04	2400.578	7305.813	−407.562	HF1-RF1
2015-06-03	10:04:04	2400.748	7305.948	−408.025	HF1-RF1
2015-06-03	10:05:05	2399.484	7305.968	−408.466	HF1-RF1
2015-06-03	13:49:49	2398.972	7305.627	−408.463	HF1-RF2
2015-06-03	13:49:49	2400.333	7305.038	−407.973	HF1-RF2
2015-06-03	13:49:49	2400.853	7305.039	−407.986	HF1-RF2
2015-06-03	13:49:49	2399.456	7304.882	−409.517	HF1-RF2
2015-06-03	13:50:50	2399.607	7306.120	−408.404	HF1-RF2
2015-06-03	13:50:50	2401.281	7303.940	−407.947	HF1-RF2
2015-06-03	13:50:50	2401.317	7304.021	−407.654	HF1-RF2
2015-06-03	13:50:50	2401.749	7303.433	−407.757	HF1-RF2
2015-06-03	13:50:50	2402.322	7303.721	−407.360	HF1-RF2
2015-06-03	13:51:51	2401.772	7303.594	−407.685	HF1-RF2
2015-06-03	14:32:32	2398.059	7304.397	−410.088	HF1-RF3
2015-06-03	14:32:32	2401.125	7303.797	−408.046	HF1-RF3
2015-06-03	14:32:32	2400.933	7304.482	−407.592	HF1-RF3
2015-06-03	14:32:32	2401.791	7303.665	−407.513	HF1-RF3
2015-06-03	14:32:32	2400.423	7305.099	−408.689	HF1-RF3
2015-06-03	14:32:32	2399.015	7306.941	−408.433	HF1-RF3
2015-06-03	14:32:32	2401.864	7303.731	−407.519	HF1-RF3
2015-06-03	14:32:32	2401.314	7304.013	−407.632	HF1-RF3
2015-06-03	14:32:32	2399.195	7306.195	−408.610	HF1-RF3
2015-06-03	14:33:33	2401.578	7303.064	−408.541	HF1-RF3
2015-06-03	14:33:33	2401.872	7301.598	−408.432	HF1-RF3
2015-06-03	14:35:35	2403.073	7302.844	−407.414	HF1-RF3
2015-06-03	14:53:53	2400.283	7306.077	−407.360	HF1-RF4
2015-06-03	14:54:54	2399.143	7305.329	−409.531	HF1-RF4
2015-06-03	14:54:54	2401.275	7304.299	−407.519	HF1-RF4
2015-06-03	14:55:55	2399.401	7302.802	−410.563	HF1-RF4
2015-06-03	15:21:21	2400.829	7305.069	−408.162	HF1-RF5
2015-06-03	15:21:21	2399.009	7305.330	−409.084	HF1-RF5
2015-06-03	15:21:21	2400.923	7306.915	−407.010	HF1-RF5
2015-06-03	15:21:21	2401.484	7304.545	−407.651	HF1-RF5
2015-06-03	15:22:22	2401.515	7303.833	−407.618	HF1-RF5
2015-06-03	15:22:22	2401.571	7303.850	−407.752	HF1-RF5
2015-06-03	15:22:22	2399.889	7307.075	−407.713	HF1-RF5
2015-06-03	15:22:22	2400.106	7304.464	−408.716	HF1-RF5
2015-06-03	15:22:22	2400.156	7303.982	−409.809	HF1-RF5
2015-06-03	15:22:22	2399.052	7307.143	−408.428	HF1-RF5

Table A1 *(Continued)*

Date	Time	*X*	*Y*	*Z*	Fracture
2015-06-03	15:22:22	2402.296	7303.653	−407.224	HF1-RF5
2015-06-03	15:22:22	2401.908	7303.616	−407.022	HF1-RF5
2015-06-03	15:22:22	2400.458	7304.952	−407.627	HF1-RF5
2015-06-03	15:22:22	2399.001	7306.923	−407.874	HF1-RF5
2015-06-03	15:22:22	2398.790	7306.970	−408.694	HF1-RF5
2015-06-03	15:22:22	2399.239	7307.149	−408.261	HF1-RF5
2015-06-03	15:22:22	2401.838	7303.314	−407.562	HF1-RF5
2015-06-03	15:22:22	2401.006	7305.038	−408.180	HF1-RF5
2015-06-03	15:22:22	2399.662	7306.987	−408.027	HF1-RF5
2015-06-03	15:23:23	2400.914	7302.725	−408.372	HF1-RF5
2015-06-04	07:17:17	2401.480	7308.627	−408.770	HF2-F
2015-06-04	07:24:24	2400.660	7307.649	−409.277	HF2-F
2015-06-04	07:24:24	2400.638	7307.551	−409.265	HF2-F
2015-06-04	07:24:24	2400.738	7307.619	−409.482	HF2-F
2015-06-04	07:25:25	2401.385	7306.816	−408.881	HF2-F
2015-06-04	07:25:25	2401.071	7306.507	−409.304	HF2-F
2015-06-04	07:25:25	2401.360	7306.868	−408.351	HF2-F
2015-06-04	07:25:25	2401.463	7306.965	−408.739	HF2-F
2015-06-04	07:42:42	2401.018	7306.905	−409.716	HF2-RF1
2015-06-04	07:42:42	2401.115	7307.052	−409.144	HF2-RF1
2015-06-04	07:43:43	2400.102	7307.147	−409.548	HF2-RF1
2015-06-04	07:43:43	2401.092	7306.866	−409.400	HF2-RF1
2015-06-04	07:43:43	2399.979	7307.134	−409.013	HF2-RF1
2015-06-04	07:46:46	2399.605	7305.837	−409.377	HF2-RF1
2015-06-04	08:13:13	2401.211	7307.188	−408.973	HF2-RF3
2015-06-04	08:13:13	2400.454	7306.541	−410.447	HF2-RF3
2015-06-04	08:13:13	2400.905	7307.789	−408.486	HF2-RF3
2015-06-04	08:14:14	2400.987	7308.396	−407.336	HF2-RF3
2015-06-04	08:14:14	2399.806	7307.195	−409.419	HF2-RF3
2015-06-04	08:14:14	2401.472	7307.211	−408.391	HF2-RF3
2015-06-04	08:14:14	2413.157	7277.910	−394.584	HF2-RF3
2015-06-04	08:14:14	2399.923	7307.087	−409.477	HF2-RF3
2015-06-04	08:14:14	2402.217	7307.830	−406.753	HF2-RF3
2015-06-04	08:14:14	2402.568	7307.693	−406.454	HF2-RF3
2015-06-04	08:14:14	2401.951	7306.755	−409.494	HF2-RF3
2015-06-04	08:14:14	2402.925	7307.131	−406.851	HF2-RF3
2015-06-04	08:14:14	2399.963	7306.043	−409.832	HF2-RF3
2015-06-04	08:15:15	2402.044	7305.482	−409.955	HF2-RF3
2015-06-04	08:15:15	2405.345	7304.963	−404.960	HF2-RF3
2015-06-04	08:15:15	2399.877	7306.042	−409.940	HF2-RF3
2015-06-04	08:16:16	2399.945	7305.930	−409.834	HF2-RF3
2015-06-04	08:33:33	2401.868	7306.913	−407.791	HF2-RF4
2015-06-04	08:33:33	2400.392	7307.161	−407.357	HF2-RF4
2015-06-04	08:33:33	2400.793	7307.060	−409.045	HF2-RF4
2015-06-04	08:33:33	2402.182	7306.854	−407.936	HF2-RF4
2015-06-04	08:33:33	2402.064	7307.272	−407.388	HF2-RF4
2015-06-04	08:33:33	2401.380	7307.091	−408.613	HF2-RF4
2015-06-04	08:34:34	2402.307	7306.880	−407.801	HF2-RF4
2015-06-04	08:34:34	2399.893	7307.241	−409.663	HF2-RF4
2015-06-04	08:34:34	2393.888	7300.638	−414.745	HF2-RF4
2015-06-04	08:34:34	2401.563	7306.509	−408.386	HF2-RF4
2015-06-04	08:34:34	2402.918	7307.494	−406.371	HF2-RF4
2015-06-04	08:34:34	2399.869	7306.059	−409.937	HF2-RF4
2015-06-04	08:34:34	2399.947	7305.943	−409.832	HF2-RF4
2015-06-04	08:34:34	2399.505	7305.613	−409.715	HF2-RF4
2015-06-04	08:35:35	2399.090	7306.157	−409.110	HF2-RF4
2015-06-04	08:35:35	2399.602	7305.687	−409.984	HF2-RF4
2015-06-04	08:35:35	2399.620	7305.687	−409.803	HF2-RF4
2015-06-04	08:35:35	2404.462	7304.898	−406.171	HF2-RF4
2015-06-04	08:35:35	2399.862	7304.993	−410.057	HF2-RF4
2015-06-04	08:35:35	2399.176	7305.577	−409.432	HF2-RF4
2015-06-04	08:36:36	2399.287	7305.638	−409.855	HF2-RF4
2015-06-04	08:49:49	2402.840	7307.520	−406.198	HF2-RF5
2015-06-04	08:49:49	2402.369	7306.716	−407.621	HF2-RF5
2015-06-04	08:49:49	2402.589	7307.083	−402.983	HF2-RF5

Table A1 *(Continued)*

Date	Time	*X*	*Y*	*Z*	Fracture
2015-06-04	08:49:49	2402.390	7307.663	−406.650	HF2-RF5
2015-06-04	08:49:49	2403.222	7306.983	−405.937	HF2-RF5
2015-06-04	08:49:49	2402.471	7306.806	−407.216	HF2-RF5
2015-06-04	08:49:49	2401.252	7306.978	−409.450	HF2-RF5
2015-06-04	08:49:49	2403.233	7306.809	−406.293	HF2-RF5
2015-06-04	08:49:49	2402.529	7307.839	−406.893	HF2-RF5
2015-06-04	08:50:50	2403.614	7306.796	−405.439	HF2-RF5
2015-06-04	08:50:50	2403.324	7306.884	−406.225	HF2-RF5
2015-06-04	08:50:50	2403.119	7307.109	−406.511	HF2-RF5
2015-06-04	08:50:50	2402.609	7307.825	−406.050	HF2-RF5
2015-06-04	08:50:50	2403.094	7306.258	−407.564	HF2-RF5
2015-06-04	08:50:50	2403.000	7306.913	−406.815	HF2-RF5
2015-06-04	08:50:50	2403.056	7306.927	−406.356	HF2-RF5
2015-06-04	08:50:50	2402.676	7306.642	−407.667	HF2-RF5
2015-06-04	08:50:50	2402.608	7306.618	−407.653	HF2-RF5
2015-06-04	08:50:50	2402.937	7307.543	−405.870	HF2-RF5
2015-06-04	08:50:50	2403.295	7307.851	−405.420	HF2-RF5
2015-06-04	08:50:50	2403.442	7306.952	−405.897	HF2-RF5
2015-06-04	08:50:50	2402.917	7307.697	−405.676	HF2-RF5
2015-06-04	08:50:50	2402.699	7307.183	−404.988	HF2-RF5
2015-06-04	08:50:50	2401.670	7306.994	−408.513	HF2-RF5
2015-06-04	08:50:50	2403.621	7306.676	−406.073	HF2-RF5
2015-06-04	08:50:50	2402.092	7308.837	−406.574	HF2-RF5
2015-06-04	08:50:50	2403.156	7308.126	−404.621	HF2-RF5
2015-06-04	08:50:50	2403.303	7308.191	−404.812	HF2-RF5
2015-06-04	08:50:50	2403.213	7306.315	−407.331	HF2-RF5
2015-06-04	08:50:50	2403.197	7308.118	−404.525	HF2-RF5
2015-06-04	08:50:50	2402.696	7307.788	−405.114	HF2-RF5
2015-06-04	08:50:50	2402.176	7308.859	−405.264	HF2-RF5
2015-06-04	08:50:50	2402.405	7307.592	−405.597	HF2-RF5
2015-06-04	08:50:50	2403.637	7307.443	−404.631	HF2-RF5
2015-06-04	08:51:51	2403.068	7306.254	−407.227	HF2-RF5
2015-06-04	08:51:51	2401.552	7305.527	−409.890	HF2-RF5
2015-06-04	08:51:51	2402.956	7306.961	−406.733	HF2-RF5
2015-06-04	08:51:51	2399.954	7306.072	−409.850	HF2-RF5
2015-06-04	08:51:51	2399.789	7305.894	−409.768	HF2-RF5
2015-06-04	08:51:51	2402.072	7305.266	−408.963	HF2-RF5
2015-06-04	08:51:51	2399.882	7306.006	−409.868	HF2-RF5
2015-06-04	08:51:51	2399.452	7305.729	−409.796	HF2-RF5
2015-06-04	08:51:51	2399.421	7305.630	−409.830	HF2-RF5
2015-06-04	08:51:51	2399.541	7305.650	−409.833	HF2-RF5
2015-06-04	08:51:51	2399.900	7306.061	−409.877	HF2-RF5
2015-06-04	08:52:52	2399.458	7305.517	−409.938	HF2-RF5
2015-06-04	08:52:52	2399.443	7305.297	−410.013	HF2-RF5
2015-06-04	08:52:52	2399.250	7305.412	−410.278	HF2-RF5
2015-06-04	08:52:52	2399.262	7305.473	−409.895	HF2-RF5
2015-06-04	08:53:53	2399.231	7305.454	−409.891	HF2-RF5
2015-06-04	12:53:53	2402.144	7311.195	−408.057	HF3-RF3
2015-06-04	13:05:05	2403.835	7311.259	−407.510	HF3-RF4
2015-06-04	13:05:05	2404.750	7309.547	−407.535	HF3-RF4
2015-06-04	13:05:05	2403.840	7311.605	−407.996	HF3-RF4
2015-06-04	13:05:05	2404.554	7310.896	−407.388	HF3-RF4
2015-06-04	13:05:05	2403.078	7311.914	−407.790	HF3-RF4
2015-06-04	13:05:05	2402.510	7311.899	−408.891	HF3-RF4
2015-06-04	13:05:05	2403.802	7311.320	−407.684	HF3-RF4
2015-06-04	13:06:06	2404.499	7311.492	−407.907	HF3-RF4
2015-06-04	13:06:06	2404.324	7310.562	−407.892	HF3-RF4
2015-06-04	13:06:06	2404.999	7311.463	−407.017	HF3-RF4
2015-06-04	13:06:06	2402.645	7310.087	−407.411	HF3-RF4
2015-06-04	13:06:06	2402.309	7310.216	−408.207	HF3-RF4
2015-06-04	13:06:06	2405.021	7311.685	−407.155	HF3-RF4
2015-06-04	13:06:06	2403.740	7311.236	−407.815	HF3-RF4

Table A1 *(Continued)*

Date	Time	*X*	*Y*	*Z*	Fracture
2015-06-04	13:06:06	2404.657	7310.885	−407.295	HF3-RF4
2015-06-09	12:52:52	2406.945	7313.687	−407.033	HF4-F
2015-06-11	14:01:01	2412.105	7320.575	−406.173	HF6-F
2015-06-11	14:01:01	2411.201	7321.974	−405.464	HF6-F
2015-06-11	14:01:01	2411.479	7321.578	−405.869	HF6-F
2015-06-11	14:01:01	2411.369	7321.702	−405.668	HF6-F
2015-06-11	14:01:01	2410.543	7322.763	−404.610	HF6-F
2015-06-11	14:02:02	2411.438	7321.739	−406.036	HF6-F
2015-06-11	14:02:02	2410.235	7321.761	−407.381	HF6-F
2015-06-11	14:02:02	2411.193	7321.400	−407.180	HF6-F
2015-06-11	14:02:02	2412.698	7319.786	−405.348	HF6-F
2015-06-11	14:02:02	2412.835	7319.838	−405.804	HF6-F
2015-06-11	14:02:02	2410.591	7320.997	−407.855	HF6-F
2015-06-11	14:02:02	2411.874	7320.320	−406.357	HF6-F
2015-06-11	14:02:02	2410.025	7323.707	−404.845	HF6-F
2015-06-11	14:02:02	2412.829	7319.897	−405.440	HF6-F
2015-06-11	14:02:02	2410.367	7322.983	−404.797	HF6-F
2015-06-12	07:39:39	2410.603	7322.877	−407.219	HF6-RF1
2015-06-12	07:40:40	2410.146	7322.588	−407.898	HF6-RF1
2015-06-12	07:40:40	2410.481	7322.950	−407.159	HF6-RF1
2015-06-12	07:40:40	2409.815	7323.009	−404.756	HF6-RF1
2015-06-12	07:40:40	2412.405	7320.318	−405.075	HF6-RF1
2015-06-12	08:07:07	2410.237	7323.361	−407.200	HF6-RF2
2015-06-12	08:08:08	2409.825	7323.102	−404.796	HF6-RF2
2015-06-12	08:08:08	2410.828	7320.877	−406.443	HF6-RF2
2015-06-12	08:08:08	2408.882	7322.555	−411.790	HF6-RF2
2015-06-12	08:08:08	2410.738	7320.907	−404.913	HF6-RF2
2015-06-12	08:25:25	2409.240	7323.065	−406.588	HF6-RF3
2015-06-12	08:25:25	2409.711	7322.970	−407.576	HF6-RF3
2015-06-12	08:25:25	2409.923	7322.762	−405.982	HF6-RF3